Interner Bericht
DESY F15-89-03
September 1989

B Meson Decays to $D\pi$ and $D\pi\pi$

by

Steven Ball

B Meson Decays to $D\pi$ and $D\pi\pi$

by

Steven Ball

Submitted to the Department of Physics and Astronomy and the Faculty of the Graduate School of the University of Kansas in partial fulfillment of the requirements for the degree of Doctor of Philosophy.

Dissertation Committee:

Raymond G. Ammar
Chairman

Date Defended: May 1, 1989

Abstract

The decays $\bar{B} \to D\pi$ and $\bar{B} \to D\pi\pi$ are observed in data taken by the ARGUS detector at the e^+e^- storage ring DORIS II. The data sample includes 100 pb^{-1} collected at the $\Upsilon(4S)$ resonance and 31 pb^{-1} continuum data taken at a center-of-mass energy just below the $\Upsilon(4S)$.

The decays $\bar{B} \to D\rho^-$ are observed for the first time. We find:

- $BR(B^- \to D^0\rho^-) = (2.0 \pm 0.7 \pm 0.7)\%$
- $BR(\bar{B}^0 \to D^+\rho^-) = (2.7 \pm 1.0 \pm 1.0)\%$.

These branching ratios are substantially larger than those for the decays $\bar{B} \to D\pi^-$, for which we find:

- $BR(B^- \to D^0\pi^-) = (0.19 \pm 0.10 \pm 0.06)\%$
- $BR(\bar{B}^0 \to D^+\pi^-) = (0.35 \pm 0.14 \pm 0.12)\%$.

Suggestive, yet inconclusive evidence is found for the existence of the decays $\bar{B} \to D^0\rho(1600)^-$". An upper limit of 0.3% at a 90% confidence level is found for the "color-suppressed" decay $\bar{B}^0 \to D^0\rho^0$.

The measured branching ratios of the decays $\bar{B} \to D\pi, D\pi\pi$ are consistent with other measurements and with theoretical predictions based upon a spectator decay model. Strong effects appear to be minor in B decays beyond the confinement in hadrons, whereas dynamical effects of the $V-A$ weak interaction are quite pronounced.

Acknowledgements

I'm thankful for the special friendships with many students at Kansas and at DESY that developed as we worked along side each other. I learned much from Joe Gress during my first two years; by doing such careful work he was a needed role model for me. Xiao Liu, or simply Liu as I know him, was often a friend in need and remains a good friend. At DESY many students extended friendship to me. A special thanks is well deserved by Klaus Reim and Manfred Paulini for associating so much with me.

Many collaborators were instrumental in helping me to start the research. I'm indebted to those who contributed to the building of the ARGUS detector. I'm truly appreciative of the software made available by many, especially Hartwig Albrecht, who also pioneered B reconstruction. Providing technical advice, our Kansas postdoc Don Coppage helped me get over what can be described as the language barrier and culture shock one experiences when first entering the environs of high energy physics research.

A warm note of appreciation goes to Herr Schmidt-Parzefall, our group spokesman, for his vote of confidence in me. I also thank Henning Schröder for his friendly advice and intelligent comments. The criticism of Michael Danilov has eventually become appreciated; we all must face a trial by fire.

I benefitted greatly from the input of several professors. Doug McKay, among others, helped me to begin with a solid theoretical foundation. Nowhan Kwak inspired me, suggested the thesis topic, and encouraged me along the way. Ray Ammar was my chief advisor and gave me many crucial words of advice. I am grateful to all of them.

Finally, the constant support of my brother, Mom, and Dad, enabled me to devote so much time and energy to this work. The Lord has provided in all trials and circumstances.

Contents

List of Figures

Chapter 1

Introduction

Objectives of the ARGUS experiment

The primary objective of ARGUS has been to investigate the physics of the b-quark, particularly through the weak decays of the B meson. The experiment has also provided valuable information on charmed particles, τ decays, and $\gamma\gamma$ interactions. While B meson studies are still in an early stage, they have proven to be a useful probe of the fundamental interactions. A clear need exists for additional measurements of B meson decays. This thesis presents a study of B meson decays to $D\pi$ and $D\pi\pi$.

Brief history of b-quark studies

The existence of the b-quark was inferred from the discovery of the Υ resonances, first observed in a 1977 Fermilab experiment [1] through the the reaction

$$p + \left\{ \begin{array}{c} Be \\ Cu \\ Pt \end{array} \right\} \to \mu^+\mu^- + X.$$

A broad peak was observed in the $\mu^+\mu^-$ invariant mass which could best be fit with three resonances narrower than the resolution. Entirely analogous to the ψ resonances which were interpreted as $c\bar{c}$ bound states, the new resonances were

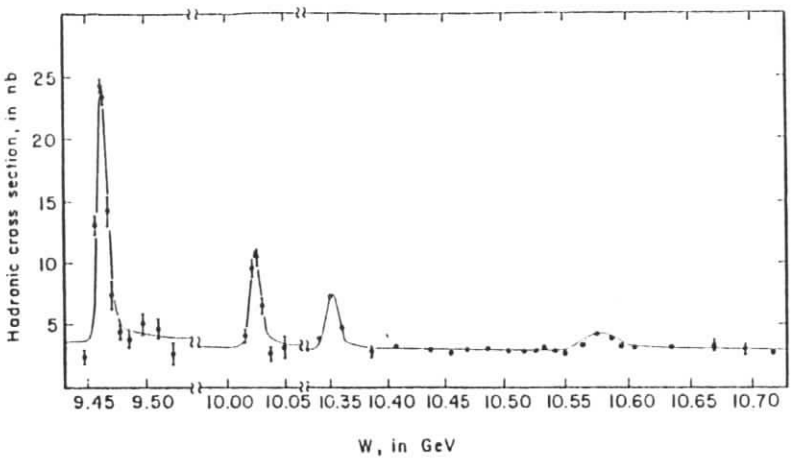

Figure 1.1: Total hadronic cross section as a function of e^+e^- center-of-mass energy [3].

identified as $b\bar{b}$ bound states with the quarks in a $^{2S+1}L_J = {}^3S_1$ configuration, leading to the observed quantum numbers $J^P = 1^-$.

The experimental setting quickly changed to the e^+e^- colliders where the $b\bar{b}$ pairs could be produced cleanly through e^+e^- annihilation, particularly favorable at the storage rings DORIS II (DOpple RIng Speicher), part of the DESY (Deutsches Elektronen SYnchrotron) facilities in Hamburg, West Germany, and CESR (Cornell Electron Storage Ring), located in Ithaca, New York, where the $b\bar{b}$ resonances are produced at rest in the lab frame. The first three Υ resonances were found to have natural widths narrower than the experimental resolution [2,3], as expected from OZI-suppression [4], yielding only decay products with zero b quantum number. In 1980, the fourth Υ resonance was observed in the visible hadronic cross section [3], shown in Figure 1, and was found to have a natural width, $\Gamma = 24 \pm 2$ MeV [5], larger than the resolution, indicating a strong decay into a meson pair containing a b and a $\bar{b}$ quark respectively. These

mesons, aptly named B mesons, could then be studied through the only process known to violate flavor, that is through weak decays. Thus the $\Upsilon(4S)$ is an ideal source for studying the weak decays of the b-quark.

The standard electro-weak model

To understand the mechanism of the b-quark decay one must begin with the unified description of the weak and electromagnetic interactions, the basis of the standard model. The fields that mediate electro-weak interactions between the elementary particles were shown to obey the principle of gauge invariance. The unified field theory, $SU_L(2)\otimes U_Y(1)$, describes the massless fields B^i_μ and A_μ as the generators of rotations in the $SU_L(2)$ space of weak isospin and the $U_Y(1)$ space of hypercharge respectively. All of the known elementary spin $\frac{1}{2}$ fermions have $SU_L(2)$ doublet partners and form generations of leptons and quarks as shown.

$$\begin{pmatrix} \nu_e \\ e \end{pmatrix}\begin{pmatrix} \nu_\mu \\ \mu \end{pmatrix}\begin{pmatrix} \nu_\tau \\ \tau \end{pmatrix} \qquad \begin{pmatrix} u \\ d' \end{pmatrix}\begin{pmatrix} c \\ s' \end{pmatrix}\begin{pmatrix} t \\ b' \end{pmatrix}$$

The massless symmetry of the fields required by renormalizability of the interactions is broken through interaction with the Higgs field, also a doublet in $SU_L(2)$. The neutral B^3_μ and A_μ fields mix to yield the physical fields of the neutral current interactions: the electromagnetic field A_μ and the massive weak field Z^0_μ. The B^1_μ and B^2_μ fields also aquire mass and can be appropriately combined to yield the physical $W^\pm_\mu$ fields, which act as the raising and lowering operators in $SU_L(2)$ space and are the only flavor changing currents allowed in the minimal Higgs model. The massiveness of the three weak vector bosons explains the relatively long lifetime of only weakly decaying particles since the propagator is inversely proportional to the square of the mediating boson's mass in the low energy regime. But because the eigenstates of $SU_L(2)$ weak isospin are not eigenstates of definite physical mass, the quarks forming

the eigenstates of $SU_L(2)$ weak doublets are related to the physical quarks by the unitary transformations which diagonalize the mass matrices. Since these transformations differ for the upper and lower quark members, a mixing matrix remains in the weak charged current which mediates transitions between them, thus the reason for the primes on the lower quark members shown above.

The hamiltonian of the charged current interaction is then

$$H_W = \frac{G_F}{\sqrt{2}} J_\mu^\dagger J^\mu + h.c.$$

where G_F is the conventional fermi constant. The current J_μ contains both the lepton and quark currents which are:

$$J_\mu^{lepton} = \left(\begin{array}{ccc} \bar{\nu_e} & \bar{\nu_\mu} & \bar{\nu_\tau} \end{array} \right) \gamma_\mu (1 - \gamma_5) \left(\begin{array}{c} e \\ \mu \\ \tau \end{array} \right)$$

and

$$J_\mu^{quark} = \left(\begin{array}{ccc} \bar{u} & \bar{c} & \bar{t} \end{array} \right) \gamma_\mu (1 - \gamma_5) \left(\begin{array}{ccc} V_{ud} & V_{us} & V_{ub} \\ V_{cd} & V_{cs} & V_{cb} \\ V_{td} & V_{ts} & V_{tb} \end{array} \right) \left(\begin{array}{c} d \\ s \\ b \end{array} \right)$$

where V_{ij} are the elements of the Kobayashi-Maskawa mixing matrix [7], hereafter referred to as the KM matrix.

The KM matrix elements V_{cb} and V_{ub} govern the transition rates for $b \to c$ and $b \to u$ respectively. Since the t-quark is far more massive than the b-quark, energy conservation allows only virtual $b \to t$ transitions, the process believed to play an important role in the large $B^0 \bar{B}^0$ mixing [8]. Though the b-quark is quite massive relative to the quarks of the first two generations, it has an amazingly long lifetime, $\tau_b = (1.18 \pm 0.14) \times 10^{-12} sec$ [9], longer than that of any hadron containing a valence c-quark. This can be explained by the relatively small KM mixing between the third generation and the first two. Inclusive and exclusive B decay measurements have already led to model-dependent calculations of $|V_{cb}|$

and upper limits on $|V_{ub}|$, favoring a dominance of $b \to c$ transitions in B decays with $|V_{cb}| \approx 0.05$.

Decays of B mesons - strong interaction effects

The model dependence in calculations of B decay rates arises from the incompletely understood influence of strong interactions. These effects are more pronounced in purely hadronic decays than in semileptonic ones. Thus measurements of hadronic decays can provide much useful information on strong interaction effects. Non-spectator effects are expected to be small in B decays due to large helicity suppression and the predicted small size of the form factor f_B. Although the so-called spectator model derives its name from the inertness of the spectator quark with regard to the weak interaction, the strong interactions between all initial and final state quarks must be taken into account. Perturbative QCD is used to include the short distance effects of hard gluon exchange while potential models are used at long distance where hadron formation finally shields off further strong effects. The connection between the quark and hadron level pictures is still quite ambiguous due to the non-perturbative nature of hadron physics and is thus subject to a variety of theoretical approaches. But it is worthwhile to outline a method which provides a useful description of weak decays of heavy hadrons and has been used to accurately describe D decays [12].

In the decay $\bar{b} \to \bar{c} u \bar{d}$ the hamiltonian of the weak charged current can be explicitly written as

$$H_W = \frac{G_F}{\sqrt{2}} V_{ud}^* V_{cb} \bar{d}_L \gamma^\mu u_L \bar{c}_L \gamma_\mu b_L$$

where $q_L = q \frac{1 - \gamma_5}{2}$, the left-handed dirac spinor wave function of the quark q. This is put into simplified notation as

$$H_W = \frac{G_F}{\sqrt{2}} V_{ud}^* V_{cb} (\bar{d}u)(\bar{c}b)$$

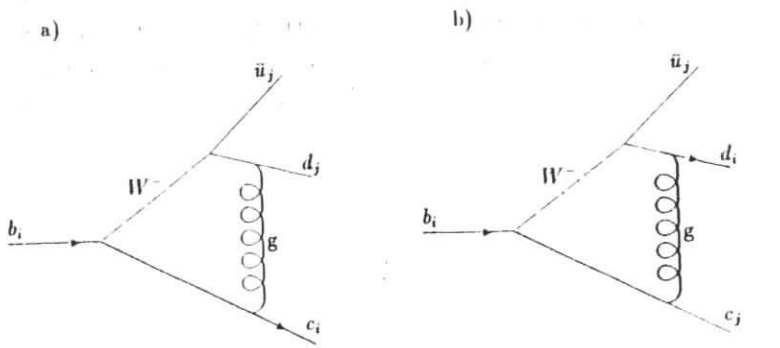

Figure 1.2: Diagrams representing a first order QCD correction to the weak hamiltonian

where the currents enclosed by parentheses are color singlets. The effect of a first order QCD correction can be shown via a Fierz transformation [11] to be equivalent to renormalizing the strength of the existing weak hamiltonian and adding a term which appears as a neutral current:

$$H_W^{QCD} = \frac{G_F}{\sqrt{2}} V_{ud}^* V_{cb} [c_1(\bar{d}u)(\bar{c}b) + c_2(\bar{c}u)(\bar{d}b)] \tag{1.1}$$

where the scale dependent coefficients at the b mass scale are $c_1 \approx 1.1$ and $c_2 \approx -0.24$. Two diagrams contributing to the respective terms in the above hamiltonian are shown in Figure 2, in which the quarks are labeled with color indices. Since gluon exchange may or may not change the color index of a quark, the color of the b-quark flows to either the c-quark (a), leaving the $\bar{u}d$ system in its original color singlet state, or to the d-quark (b), leaving the $\bar{u}c$ system in a color singlet state.

Up to this point the procedure is straightforward. The problem we now face is at long distances where non-perturbative QCD effects form color-singlet hadrons. The procedure of reference [12] is to take a somewhat phenomenological

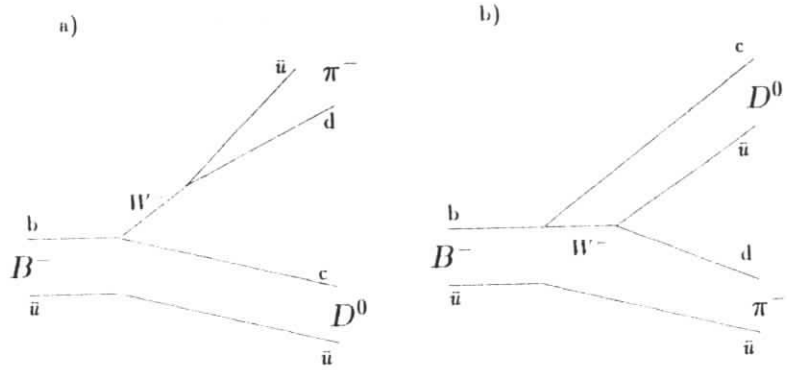

Figure 1.3: Diagrams contributing to the decay $B^- \to D^0\pi^-$

approach by assuming that factorization and the subsequent replacement of quark currents by hadron currents, can be used with some caution. For the coefficients of the resulting hamiltonian,

$$H_{eff} = \frac{G_F}{\sqrt{2}} V_{ud}^* V_{cb} [a_1(\bar{d}u)_H(\bar{c}b)_H + a_2(\bar{c}u)_H(\bar{d}b)_H], \tag{1.2}$$

assuming factorization would yield

$$a_1 \approx c_1 + \frac{c_2}{N_c} \text{ and } a_2 \approx c_2 + \frac{c_1}{N_c}$$

to first order in $1/N_c$ where N_c is the number of color charges. But due to uncertainties of order $1/N_c$ in the factorization approximation these coefficients are allowed to have a free parameter ξ such that

$$a_1 = c_1 + \xi c_2 \text{ and } a_2 = c_2 + \xi c_1.$$

The calculation of the decay $B^- \to D^0\pi^-$ actually involves both a_1 and a_2 terms, represented by the two diagrams in Figure 1.3. The a_1 term is represented by diagram (a) and is the dominant term while the a_2 term is represented by

diagram (b) which has been referred to as "color-suppressed". Quark color indices and gluon exchange are not explicitly shown, although both of the c_1 and c_2 terms of the first order QCD corrected hamiltonian (equation 1.1) contribute to each of the diagrams shown.

To determine ξ the authors of reference [12] found good agreement with much of the D decay data by using $\xi = 0$, a complete cancellation of all color-suppressed terms. This results in a destructive interference between the diagrams of a_1 and a_2, actually a Pauli-suppression due to identical quarks in the final state. This has been used to explain the lifetime difference between the D^0 and D^+ mesons [5]. Other theoretical predictions using a very similar calculation [14,16] were also motivated by this observation. A somewhat different approach, QCD sum rules [18], an attempt to include the non-factorizable amplitudes, also finds a near cancellation in many D decay modes. Unfortunately, only calculations of the first method have been used so far for exclusive B decay branching ratios. These are listed in Table 4.1 in the final chapter where they are discussed in more detail.

Motivation for $\bar{B} \to D\pi, D\pi\pi$ measurements

The massiveness of the B meson in relation to the D meson (and therefore the much larger phase space available for numerous possible decay modes) is alone responsible for roughly one order of magnitude lower branching ratios for the simple 2-body B decays relative to corresponding 2-body D decays. B decays typically yield high multiplicity final states; the mean multiplicities of final state particles are $\bar{n}_{ch} = 5.5$ and $\bar{n}_\gamma = 5.0$ [19], in contrast to D decays which have low charged multiplicities, $\bar{n}_{D^0} = 2.5$ and $\bar{n}_{D^+} = 2.2$ [20] and are mostly accounted for by resonant 2-body decays [12]. The Pauli-suppression term is not expected to cause a noticably large effect in B decays since the large amount of phase space minimizes the losses due to destructive interference.

However, the low multiplicity decays chosen for this study, while accounting for only a small fraction of all B decays, may be the most favorable ones for observing such an effect. Decays with low q^2 values for the off-shell W masses such as $\bar{B} \to D\pi^-$, have very limited phase space by the restriction that the $\bar{u}d$ quark pair have nearly parallel momenta, indicated by the small size of the form factor, $f_\pi = 133MeV$, which enters the calculation. If the charged and neutral B lifetimes are nearly equal, the interference is manifested through different branching ratios for decays such as $B^- \to D^0\pi^-$ and $\bar{B}^0 \to D^+\pi^-$, which differ only by the spectator quark. But if in fact strong effects in B decays are consistently small, one may use this as an advantage for observing effects due to the form of the electro-weak interaction. A discussion of these effects based upon the measurements of this thesis and other B decay measurements is presented in the final chapter.

Chapter 2

The ARGUS Experiment

Operation of DORIS II

The ARGUS experiment relies upon the efficient control of its electron and positron beams in the DORIS II storage ring. The sequence is illustrated in Figure 2.1. Electrons are boiled off of hot filaments and accelerated up to 50 MeV by LINAC 1 before entering the DESY synchrotron. The positrons, produced in collisions of electrons with a tungsten target, are accelerated up to 330 MeV by LINAC 2 and accumulated in the Positron Intensity Acculmulator (PIA) before entering the synchrotron. There the bunches are separately accelerated up to 5 GeV in about 20 msec before being ejected and stored in the DORIS II storage ring. This process is continued until currents of about 35 mA are accumulated in each single e^+ and e^- bunch. The normal filling time is relatively brief, only a few minutes, compared to the beam lifetimes which vary from 1 to 3 hours. Refilling is normally done every hour to retain high luminosity. The average luminosity collected per day is about $600nb^{-1}$.

During the period in which the data used for this analysis were taken, the two interaction regions of DORIS II were occupied by the ARGUS detector and the Crystal Ball detector. The sharp 12 m bending radius of the DORIS II bending magnets also produces a rich source of synchrotron radiation which is used by HASYLAB and other facilities surrounding the storage ring.

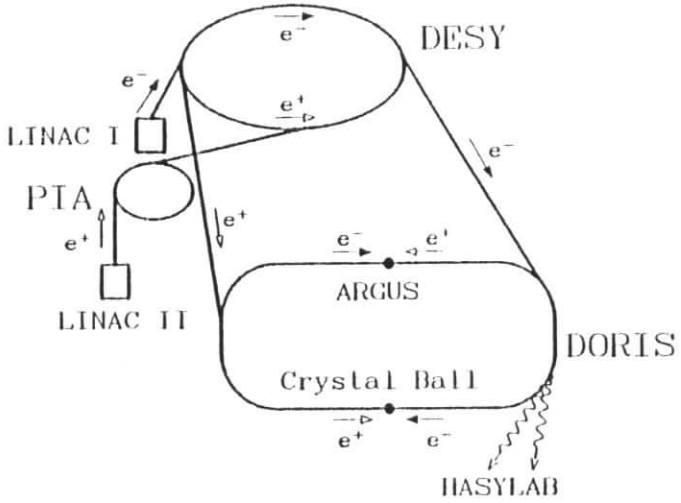

Figure 2.1: The sequence of beam supply to the DORIS II storage ring

The ARGUS detector

The ARGUS detector [23] is referred to as a universal detector due to its design to detect both charged and neutral particles over more than 90% of the 4π solid angle. A cross-section in the plane of the beam axis is shown in Figure 2.2. Its high resolution and excellent particle identification make it quite suitable for the isotropic, high multiplicity decays of the $\Upsilon(4S)$ resonance. The detector is composed of many independent components, each structured with a cylindrical symmetry with respect to the beam axis. These include a main drift chamber, a vertex chamber, a time-of-flight (TOF) system, electromagnetic shower counters, muon chambers, and a 0.8T magnet.

The heart of the ARGUS detector is the main drift chamber which provides tracking, momentum measurement, and particle identification of charged particles by specific ionization. The chamber is designed to measure a particle's transverse momentum with good resolution and to obtain a useful z momentum measurement through use of wires at small stereo angles with respect to the beam axis. The sequence of stereo angles of the 36 layers of sense wires is $0°, +\alpha, 0°, -\alpha$,etc., where α increases from 40 mrad to 80 mrad such that the maximum displacement of the sense wire from the center of the drift cell is only 1 mm. The drift cell size, 18.0×18.8 mm^2, and the gas used in the chamber, 97% propane and 3% methylal, were chosen to achieve high dE/dx resolution. The dE/dx resolution is typically 5% and its usefulness for particle identification can be ascertained from Figure 2.3a, a scatterplot of the specific ionization versus momentum. The momentum resolution was determined to be

$$\frac{\sigma_{p_t}}{p_t} = \sqrt{0.01^2 + (0.009 \times p_t(GeV))^2} \qquad (2.1)$$

where the first term is due to multiple scattering in the chamber wall and beam pipe.

The ARGUS vertex chamber was installed in the spring of 1985, considerably

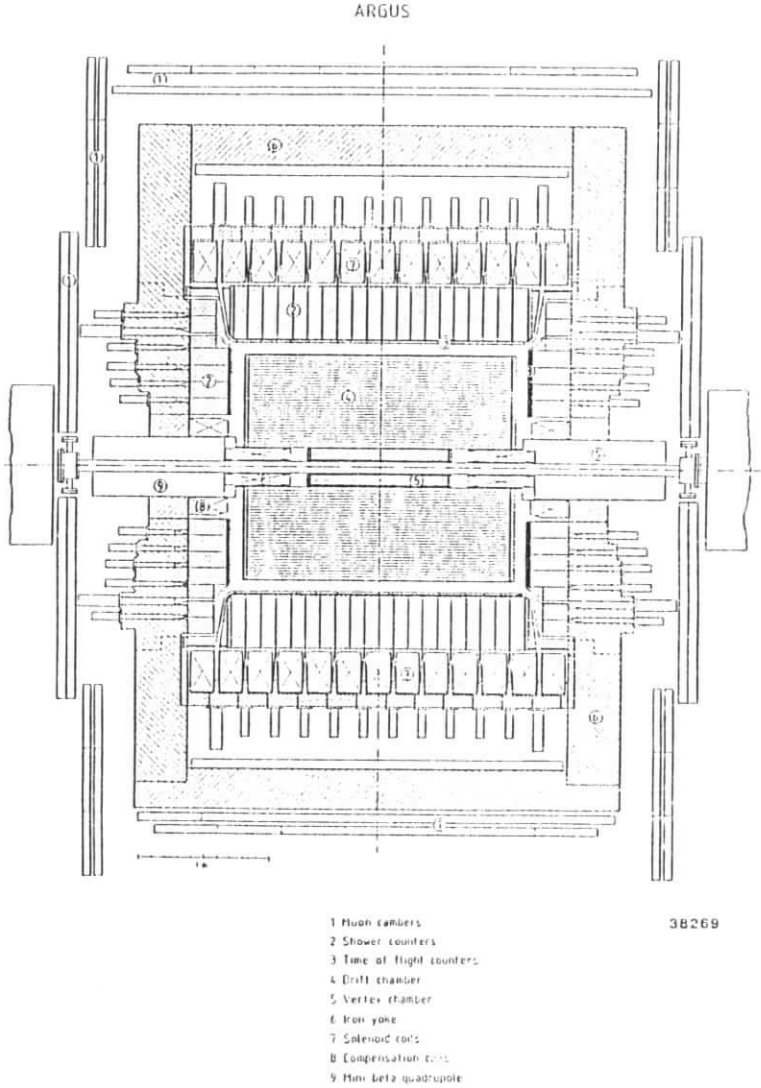

Figure 2.2: The ARGUS detector

later than the initial data-taking which began in the fall of 1982. The data used for this analysis were collected through the fall of 1986; 88% of the total luminosity collected at the $\Upsilon(4S)$ was taken with the vertex detector. Its main purpose is to improve momentum and vertex resolution. Its location between the main drift chamber inner wall and the beam pipe determined its dimensions, 1m long with inner and outer radii of 5cm and 14cm respectively. The sense wires are strictly parallel to the beam axis, arranged in a close-packed hexagonal cell pattern with each cell having an inscribed radius of 4.5mm. It is operated with CO_2 gas because of the need for a slowly rising drift velocity with increasing field strength. The spatial resolution of tracks extrapolated back to the vertex is about 100μm. The momentum resolution is improved from $\sigma_{p_t}/p_t = 0.9\%p_t$ to $\sigma_{p_t}/p_t = 0.6\%p_t$.

The main purpose of the TOF system is to provide an independent charged particle identification; it is also a major component of the fast trigger system described later. The rest mass is determined from the momentum measured by the curvature in the magnetic field of the drift chamber and the velocity measured by the TOF system using the relationship $p = \beta\gamma m_o$. The system is composed of 160 scintillation counters consisting of 64 barrel counters and 48 endcap counters. The placement of the phototubes outside of the magnet coils requires light guides which bend the light through openings in the array of shower counters as shown in Figure 2.2. The pulses received by the TDC's are used in conjunction with the bunch crossing signal (provided by electrostatic pickups in the beam pipe near the interaction point) to obtain the time-of-flight. Its 220ps resolution results in the mass resolution observed in Figure 2.3b which shows the mass^2 versus momentum. This provides a particle identification resolution comparable to that of the dE/dx measurement.

The electromagnetic shower counters are used to measure the energy and direction of photons and to identify electrons by their characteristic pattern of energy deposition. Other important functions of the shower counters include

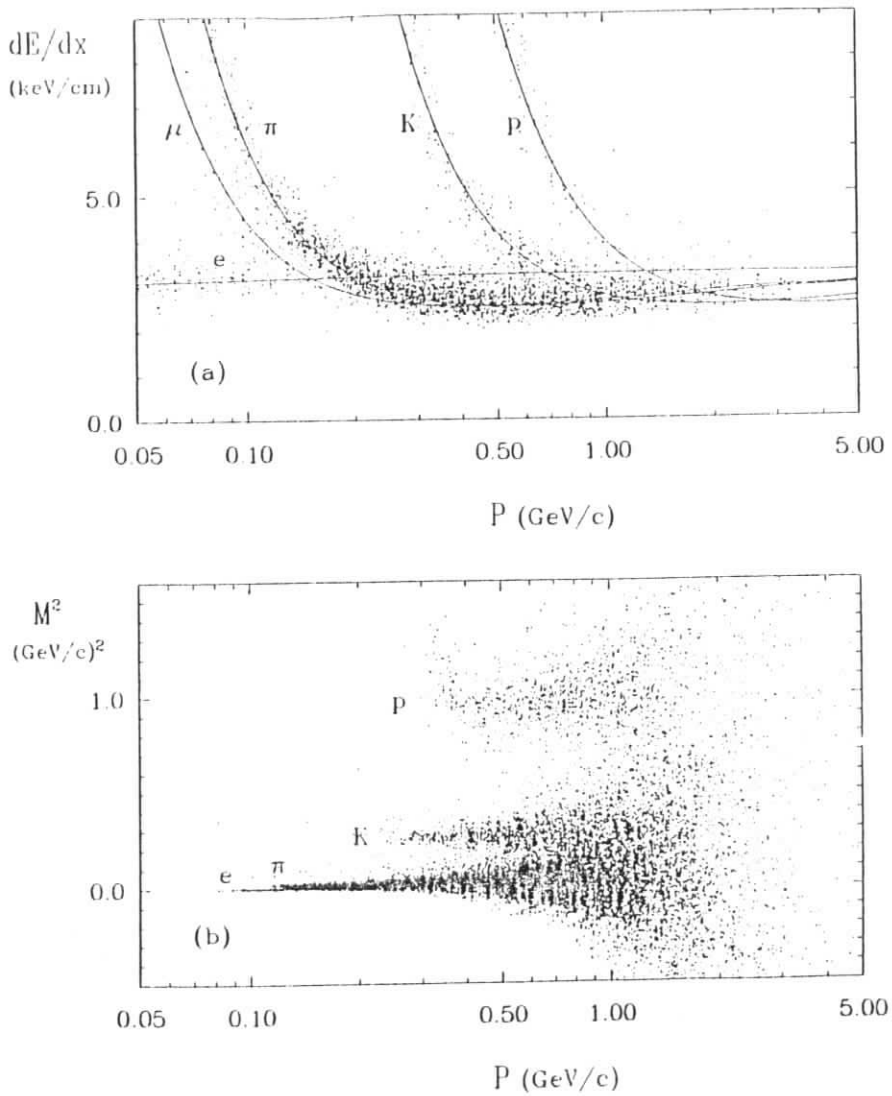

Figure 2.3: Particle identification using a) dE/dx by the drift chamber and b) time-of-flight by the TOF system.

their use in the fast trigger system and for luminosity measurement through the Bhabha event rate. The system includes 1280 barrel counters arranged in 20 rings each containing 64 counters and 240 endcap counters arranged in 5 concentric rings. Each counter is composed of alternating layers of lead and scintillator material totalling 12.5 radiation lengths whereas the total amount of material in front of the counters ranges from only 0.16 to 0.52 radiation lengths, allowing excellent detection efficiency for photons with energies as low as 50 MeV. A wavelength shifter bar extending from the front to the back along the side of each counter delivers the light pulses to the light guides leading to the phototubes outside the magnet coils. The resolution achieved by the barrel counters is

$$\frac{\sigma_E}{E} = \sqrt{0.072^2 + \frac{0.065^2}{E(GeV)}} \qquad (2.2)$$

while that of the endcap counters is slightly worse. The constant term is mainly due to losses in the support structure.

The muon chambers consist of three layers of proportional tubes, one inside the iron yoke and two outside of it. They are needed to obtain clean identification of muons, which cannot be done using only the dE/dx and TOF measurements. The innermost layer has a lower momentum cutoff of 0.7 GeV due to absorption, and covers 43% of the solid angle. The outer two layers cover 87% of the solid angle and have a lower cutoff of 1.1 GeV. The inner layer is shielded from hadrons coming from the interaction region by 3.3 absorption lengths and the outer layers by 5.1 absorption lengths, providing reasonably clean muon identification.

The magnetic field must be controlled to very high precision throughout the inner detector for the purpose of accurate momentum determination and because of the delicate beam optics system. The field lines of the nearly homogeneous 0.8T magnetic field provided by the main solenoid coils run parallel to the beam axis to induce a circular track curvature in the plane transverse to the beam axis. To offset the influence of the field in the beam pipe, compensation coils

were installed at each end of the beam pipe inside of the detector. To damp out betatron oscillations in the beam and achieve high luminosity, mini-beta quadrupoles were placed behind the compensation coils.

Trigger system

Because of the large backgrounds from cosmic rays and beam-gas and beam-wall interactions, a fast and efficient method is needed to reduce the rate of events read out to the online computer to a managable level. To accomplish this, the ARGUS trigger system is divided into two stages: a fast pretrigger which can operate within the e^+e^- bunch crossing rate of 1 MHz and a secondary trigger referred to as the "Little Track Finder" or LTF.

The pretrigger system is strictly a hardware device which utilizes only the TOF and shower counter information. Events are accepted upon satisfying one of several conditions:

- Total Energy Trigger - requires more than 700 MeV of energy deposited in each z hemisphere of shower counters.
- High Energy Shower Trigger - requires more than 1 GeV in one of 16 barrel counter groups.
- Charged Particle Pretrigger - requires at least one charged track in each z hemisphere as determined by an overlap of TOF and shower counter groups.
- Coincidence Matrix Trigger - requires same as previous trigger except that the tracks be in opposite ϕ hemispheres.
- Cosmic Trigger - requires tracks in opposite ϕ hemispheres from TOF counter groups; used for tests and background studies.
- Random Trigger - a random gate of approximately 0.1 Hz rate to all electronics; used for random noise studies.

During normal data taking all triggers except for the cosmic trigger are used as input to the pretrigger collector. A coincidence between the bunch crossing signal and one of the pretriggers is necessary to begin the secondary trigger or LTF which examines an event for evidence of charged tracks with the drift chamber and TOF information. The LTF requires software only to store a list of drift chamber wire hits into its memories where many possible sequences define a good track. As soon as the track counter exceeds a value given by the pretrigger condition the event is read out by the online computer.

Data flow

Data taken by the ARGUS detector makes the long journey from the pulses received by the individual detector components to the software format used for data analysis through a multiple step process of data reduction and transfer. From the moment an event is read out online to the point at which it can be analysed, the data flow process can be summarized by the flow chart shown in Figure 2.4, which shows both the data flow components and the methods developed to access information. The first major distinction made is between online and offline components, where online is defined by the high rate of data transfer needed until it is dumped onto tape, allowing the more time consuming offline data processing to follow later.

The online monitoring of operating parameters of the detector and electronics is provided by a MIK 11/2S mini computer. Significant deviations from nominal values will cause an alarm to occur which, depending on the severity level, may stop the data taking or issue a warning. The problem is located though a display indicating the deviant value. Normally the correct value is quickly restored and data taking resumed.

The four online data flow components following the detector serve to handle an enormous amount of data at a high rate. The signals received in each detector component are digitized by the CAMAC modules which read out the data to

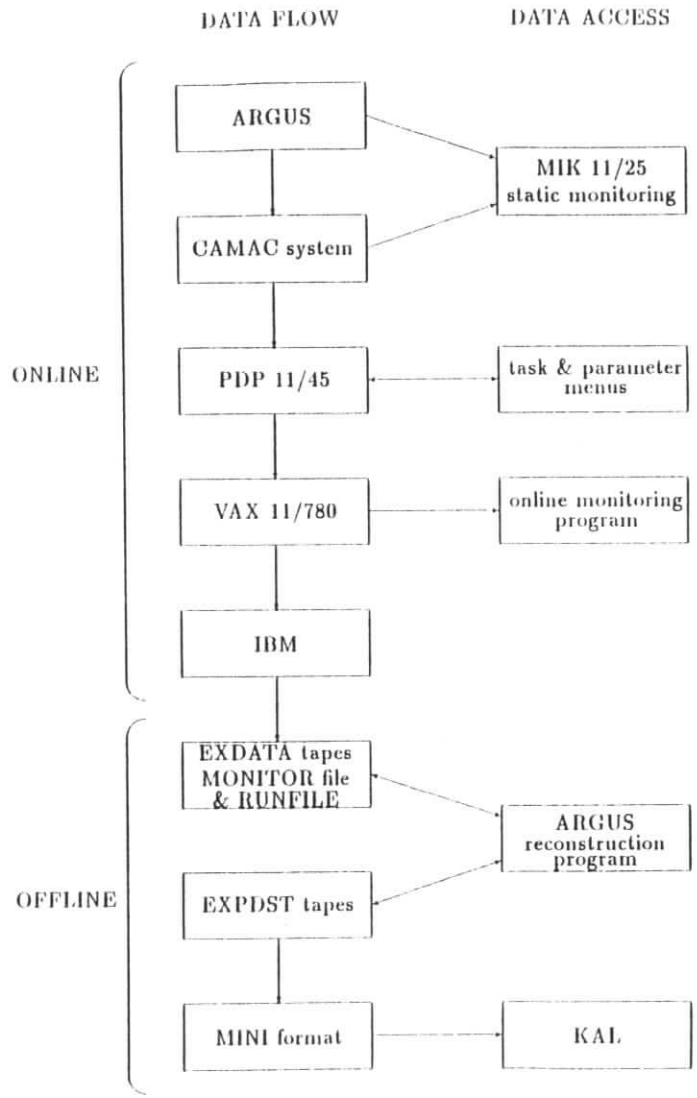

Figure 2.4: Summary of data flow and data access

the CAMAC microprocessor. There the complete event record is constructed and sent to the DEC PDP 11/45 computer. The PDP serves to synchronize the raw data flow from the various components and to allow the user control of parameters and online tasks such as calibration procedures. The data are transferred to the VAX 11/780 for the purpose of online monitoring and to ensure adequate data flow with the larger memory and processing power of the VAX. The monitor system fills various histograms which indicate details of detector performance and continuously updates run status information such as trigger rates and data transfer rates. The data are then sent to the IBM to be stored on disk. After roughly 40,000 events are accumulated the data are automatically dumped onto a tape during which the final event record format is made. Every two tapes are copied together to EXDATA tapes while calibration runs are copied onto the MONITOR file and data taking run information onto the RUNFILE. This ends the online portion of the data flow process.

The data stored on the EXDATA tapes in the form of various signals such as ADC and TDC values must be reconstructed to yield track and vertex information. The ARGUS reconstruction program begins with the drift chamber information. A pattern recognition routine first locates track candidates using only wires parallel to the beam axis. Upon including possible stereo wires a track fit routine then calculates a helical trajectory by a minimum χ^2 procedure. The track fit is iterated many times including more detector information such as the inhomogeneity of the magnetic field, remaining unassociated wires, energy loss due to specific ionization, kinks due to multiple scatter, VDC information, and finally, the vertex constraint. Vertices are also located by a minimum χ^2 procedure. Tracks with unacceptably high χ^2 values are discarded and the procedure iterated until an acceptable vertex is obtained. Since K^0_s and Λ decays often yield one track compatable with the primary vertex, a subsequent routine searches through all possible oppositely charged pairs of tracks which do not already belong to the same vertex in order to locate more possible vertices.

Charged particle identification is done using the dE/dx and TOF information together with the momentum determined from the track fit. Theoretical dE/dx values and their uncertainties are calculated for each particle hypothesis and are used to construct the χ^2 values:

$$\chi^2_i = \frac{[(\frac{dE}{dx})^{meas} - (\frac{dE}{dx})^{theo}_i]^2}{\sigma^2_{meas} + \sigma^2_{theo_i}} \qquad i = e, \mu, \pi, K, p$$

A similar χ^2 calculation is made from the TOF values. Summing both χ^2 contributions, a normalized likelihood function is constructed:

$$LH_i = \frac{w_i exp(-\chi^2_i/2)}{\sum_i w_i exp(-\chi^2_i/2)}$$

where w_i is a weight assigned to the ith mass hypothesis. The ratios of the weights are normally chosen to correspond to the relative particle abundances observed in the data. The standard set of weights, which can be chosen during data analysis, is:

e	:	μ	:	π	:	K	:	p
1	:	1	:	5	:	1	:	1

Unless otherwised specified, in order for the particle identification to be considered acceptable, $LH_i > 1\%$ is required.

Separate likelihood functions are constructed for electron and muon identification utilizing information from the shower counters and muon chambers. For electrons, the lateral spread of energy deposited in the shower counters is typically small while its total energy deposition is nearly equal to its momentum, whereas hadrons have a larger lateral spread and deposit significantly less than their total energy. Muons with $P > 1GeV$ typically deposit a very small fraction of their energy in the counters and can be traced to a muon chamber hit with high efficiency. Photon identification is done using isolated clusters of shower counters not associated with charged tracks. A calibrated energy correction routine is necessary to account for leakages and variations of collected light.

Decays of high momentum π^0's can result in two unresolved photon showers for which the correction is inappropriate; the energy of these candidates is therefore uncorrected during data analysis.

The reconstructed data are written to EXPDST (Data Summary Tapes). These data can then be used for analysis, although the amount of information and the data format make these tapes impractical for analysing a large number of events. For individual events of interest, an interactive version of the reconstruction program was developed to study the events visually. An example of its event display capabilities is shown in Figure 2.5 which contains a candidate $\bar{B}^0 \to D^+\rho^-$ decay. The view is a projection in the r-ϕ plane, showing the VDC and drift chamber hits, TOF counter hits, and deposited shower energy.

For the purposes of efficient data analysis, a fast and elegant method is possible through the use of KAL (Kinematical Analysis Language). The reconstructed data from the EXPDST's are first reduced to a MINI format which can then be read by the KAL program. Though the program is written in standard Fortran IV language, it receives as input a simplified language which greatly reduces the need for usual programming structures and provides many frequently used functions through simple statements, greatly reducing possible programming and calculation errors. Output can be accumulated in GEP (Graphical Editor Program) files in the form of plots or "n-tuples", n dimensional arrays of n variables up to n=12, which can be used to make further cuts on the data after the data processing is completed. This saves the user an enormous amount of time in analysing the data.

The total amount of data collected as of fall of 1986 is listed in Table 2.1. The data taking periods are divided into experiments which denote a period of continuous running. Each experiment is subdivided into runs which merely indicate changes in raw data tapes. Continuum data include data taken away from the Υ resonances, mostly between the $\Upsilon(3S)$ and $\Upsilon(4S)$ resonances. The small amount of experiment 3 data are usually excluded from data analysis due

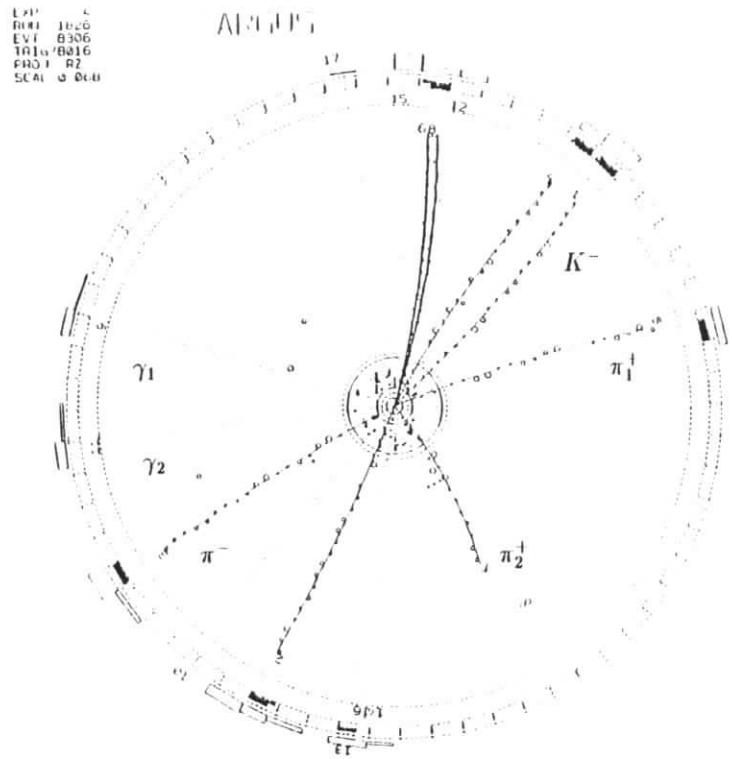

Decay Candidate

$$\bar{B}^0 \to D^+\rho^- \to \pi^-\pi^0 \to \gamma_1\gamma_2$$
$$\hookrightarrow K^-\pi_1^+\pi_2^+$$

Decay	M (GeV)	P (GeV)
$\pi^0 \to \gamma\gamma$	0.132 ± 0.016	0.548 ± 0.029
$\rho^- \to \pi^-\pi^0$	0.753 ± 0.020	2.251 ± 0.037
$D^+ \to K^-\pi^+\pi^+$	1.876 ± 0.013	2.221 ± 0.009
$\bar{B}^0 \to D^+\rho^-$	5.282 ± 0.004	0.291 ± 0.018

Figure 2.5: Display of an event with a well measured $\bar{B}^0$ candidate reconstructed through the decay $\bar{B}^0 \to D^+\rho^-$.

E_{cm*}	Integrated Luminosity (pb^{-1})				
	Exp. 2	Exp. 3	Exp. 4	Exp. 5	Total
$\Upsilon(1S)$	7.4	14.3		23.3	45.0
$\Upsilon(2S)$	36.8				36.8
$\Upsilon(4S)$	9.1	2.7	48.0	43.4	103.2
Continuum	3.4	3.9	20.1	21.8	49.2

Table 2.1: Summary of ARGUS data collected through 1986

to unstable detector conditions. The data used for this study include $100pb^{-1}$ of $\Upsilon(4S)$ data and $31pb^{-1}$ of continuum data taken at the center-of-mass energy 10.43 GeV.

Chapter 3

Analysis of the Decays $\bar{B} \rightarrow D\pi$ and $\bar{B} \rightarrow D\pi\pi$

Feasability of B reconstruction

Before deciding upon the details of the selection criteria for the analysis, the feasability of B reconstruction had to be assessed. This discussion is intended to clarify the analysis procedure. Two assessments are made: the number of B decays one can reasonably expect to reconstruct, and the level and behavior of background to be dealt with.

The $\Upsilon(4S)$ data sample of $100pb^{-1}$ is estimated to contain 93,000 $\Upsilon(4S)$ decays with an uncertainty of 10%. We assume that 45% of these decays are to $B^0\bar{B}^0$ and 55% to B^+B^-. But since we need only order of magnitude estimates, we assume about 10^5 neutral and 10^5 charged B meson decays. Hadronic B decay branching ratios have been measured to be typically 1% or less [27,28]. B reconstruction efficiencies vary from less than 1% to a few percent (reconstruction efficiencies are small since only exclusive D decay modes are used for D reconstruction, yielding D efficiencies of about 5%). Taking 1% as a typical value for the B reconstruction efficiency we do not expect to reconstruct more than roughly 10 B mesons per decay mode.

A signal of 10 events will not be evident unless the background level is low.

This level is affected by both the resolution of the signal and the effectiveness of the selection criteria in suppressing background. The mass resolution is determined by the detector resolution and the effect of kinematic fitting. Monte Carlo studies (including VDC information) indicate that the mass resolution σ_M is about 30 MeV. Even so, for actual data this is still too broad to observe such a small signal with respect to the background level. Mass constraints of intermediate decaying particles such as the D meson yield modest improvements of a few percent. A very effective kinematic constraint is possible due to the production of the $\Upsilon(4S)$ at rest. We constrain the B energy to half of the $\Upsilon(4S)$ mass of 10580 MeV [28]. The limiting factor of the resulting resolution is actually due to the beam energy spread which is about 6 MeV for DORIS II. The expected signal resolution, derived in Appendix A, is 4 MeV, nearly an order of magnitude improvement.

Background sources may come from events of the following types: QED, beam-wall, beam-gas, continuum, and $\Upsilon(4S)$ events. The first three types are highly suppressed by the following multi-hadron cuts [34]:

1. $n_{ch} + n_\gamma > 5$

2. $\frac{1}{\sqrt{s}}(\sum P^{ch} + \sum E^\gamma) > (\frac{1}{\sqrt{s}} \sum P_z^{ch})^2 \times 2.5 + 0.35$

where $\sqrt{s}$ is the center-of-mass energy and the summations are over all charged or neutral particles detected in the event. Approximately 98% of $\Upsilon(4S)$ events pass these cuts. Continuum events form the largest remaining background since these outnumber $\Upsilon(4S)$ events by about 4 to 1 in the $\Upsilon(4S)$ data sample. Although these are usually jet-like, topological cuts cannot sufficiently suppress such events without significantly hurting the B reconstruction efficiency. Instead one must resort to other criteria in order to suppress the continuum background, as discussed in the next section. Finally, there is background from the $\Upsilon(4S)$ itself which can vary from completely random selections of particles from both B decays in the event to highly correlated background in which a slow particle

is the only difference between the actual B decay and the decay for which it is analysed. The measured energy resolution must be sufficiently sharp to suppress such candidates.

Selection criteria

The specific B decay modes investigated include[1]:

$$\begin{array}{ll} B^- \to D^0\pi^- & \bar{B}^0 \to D^+\pi^- \\ \to D^0\pi^-\pi^0 & \to D^+\pi^-\pi^0 \\ \to D^+\pi^-\pi^- & \to D^0\pi^-\pi^+ . \end{array}$$

The D mesons were reconstructed through the following decay modes:

$$\begin{array}{ll} D^0 \to K^-\pi^+ & D^+ \to K^0_s\pi^+ \\ \to K^0_s\pi^+\pi^- & \to K^-\pi^+\pi^+ \\ \to K^-\pi^+\pi^-\pi^+ & \to K^0_s\pi^+\pi^-\pi^+ . \end{array}$$

According to the MARK III branching ratios [21], these modes account for 16.5% of D^0 decays and 14.0% of D^+ decays. Only D candidates with momentum less than 2.65 GeV were selected due to the kinematic limit of $x_p < 0.5$ for all particles from B decays where $x_p = p/E_B$. There is a large background from $\pi - K$ misidentification for charged K candidates above 1 GeV and an abundance of soft π's particularly in $\Upsilon(4S)$ decays. Both of these contribute to a large peaking at $cos\theta_K = 1$ where θ_K is the angle between the K and D directions in the D rest frame. Since this distribution must be flat for decays of the pseudoscalar D meson, the cut $cos\theta_K < 0.8$ enhances the signal for all D decay modes. K^0_s candidates are reconstructed through the decay $K^0_s \to \pi^+\pi^-$ with the requirement that the χ^2 of the secondary vertex to be smaller than 36. This sample is quite clean and only loose cuts are required, that the measured mass be within 30 MeV of the nominal K^0 mass and that the χ^2 be less than 36. The mass of D candidates are required to be within 50 MeV of the nominal D

[1] References to a specific charge state are to be interpreted as implying the charge conjugate state also throughout this thesis unless otherwise indicated.

mass and have a χ^2 less than 9. All nominal masses are taken from reference [5]. Mass constraints are applied on each intermediate state to improve resolution.

The π^0 candidates were reconstructed through the decay $\pi^0 \rightarrow \gamma\gamma$ in which each photon was identified from a distinct electromagnetic shower. Each photon is required to have an energy greater than 50 MeV contained in two or more adjacent shower counters in order to reduce low energy background noise. The $\gamma\gamma$ invariant mass is required to be within 50 MeV of the nominal π^0 mass and have a χ^2 less than 5 and is subsequently constrained to the π^0 mass. A second method was employed to reconstruct π^0 candidates when the two photons from an energetic π^0 merge to form a single cluster with typically large lateral spread. We define the lateral energy spread E_{lat} as $\sum_{i=3}^{n} E_i(\vec{r}_i - \vec{r})^2/\bar{r}^2$ where the index i runs over the counters in the shower cluster excluding the two with the highest deposited energy, $\vec{r}$ is the center of gravity of the shower, and $\bar{r}$ is the mean distance between two adjacent counters. We can then calculate the fractional lateral energy spread, $f_{lat} = E_{lat}/(E_{lat} + E_1 + E_2)$. To suppress single photons, single cluster π^0's must satisfy $f_{lat} \geq 0.1$ and have a total energy greater than 1 GeV. The energy and direction of the π^0 is then taken to be the energy and direction of the single cluster.

Finally, three principal cuts are applied for the B selection criteria. The first cut is chosen to suppress the large continuum background. A thrust axis is calculated for the B candidate and then for the remaining particles in the event. The angle α between thrust axes should be isotropically distributed for B decays since both B's decay nearly at rest and are thus uncorrelated. But due to the 2-jet structure of the continuum events, which have well defined thrust axes, a dominant peaking occurs at $cos\alpha = \pm 1$. Figure 3.1 shows this distribution for $D\pi$ candidates, which agrees well with the behavior observed for $D\pi$ candidates in continuum data. For $D\pi$ candidates the requirement $|cos\alpha| < 0.8$ is chosen while for $D\pi\pi$ candidates which yield a less sharply peaking behavior, the requirement $|cos\alpha| < 0.7$ is chosen.

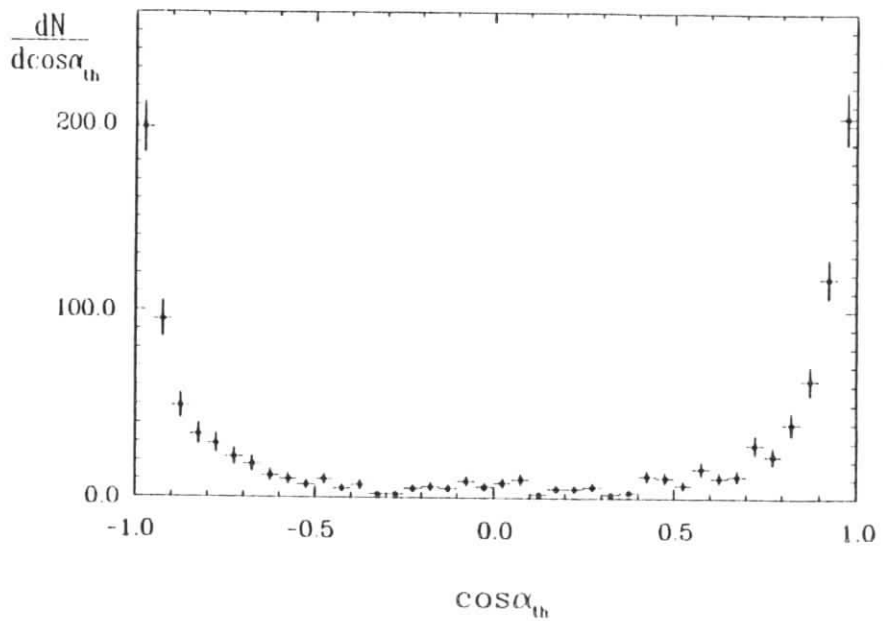

Figure 3.1: Thrust angle distribution for $D\pi$ candidates in $\Upsilon(4S)$ data

The second cut utilizes the fact that the energy of the B is the same as the beam energy E_{beam}. The measured energy E_{meas} for each $D\pi$ and $D\pi\pi$ candidate must satisfy $|E_{meas} - E_{beam}| < 2\sigma_E$ where σ_E is the measured energy resolution. For B decays with only charged particles in the final state, σ_E is typically 30 MeV; we do not accept poorly measured candidates, namely those with $\sigma_E > 60$ MeV. For the modes with a π^0, σ_E is highly correlated with the π^0 momentum due to the nearly linear rise of the shower energy resolution with energy (see equation 2.2). For these B candidates σ_E is typically 45 MeV for π^0 momenta less than 900 MeV; those with $\sigma_E > 300$ MeV are rejected. Subsequent to the energy cut, an energy constraint is performed on the B candidate, resulting in a 4 MeV mass resolution.

The third cut utilizes the detector information in a coherent fashion in order to make a quality cut on candidates and to provide a tool for dealing with events with multiple entries. A total probability is calculated from the sum of all χ^2 contributions from particle identification and kinematic constraints and it is required to be greater than 1% for all modes. Multiple entries which arise mainly from the exchange of low momentum particles in the decay chain or in the event, are suppressed by limiting the analysis to the candidate with the highest total probability. Appendix B describes some of the corrections associated with this selection method.

Analysis results

The decay modes $B^- \to D^0\pi^-$ and $\bar{B}^0 \to D^+\pi^-$ are relatively clean due to the distinctive back to back momenta of the D and π at nearly 2.3 GeV. Figure 3.2a shows the scatterplot of the D momentum versus the invariant mass of the $D\pi$ system of all $D\pi$ candidates. The dashed line indicates the kinematic boundary. kinematically allowed region. A clustering of events centered at a D momentum of 2.3 GeV and $D\pi$ mass of 5.28 GeV is clear evidence for this decay. The projection of all candidates onto the mass axis is shown below in Figure 3.2b.

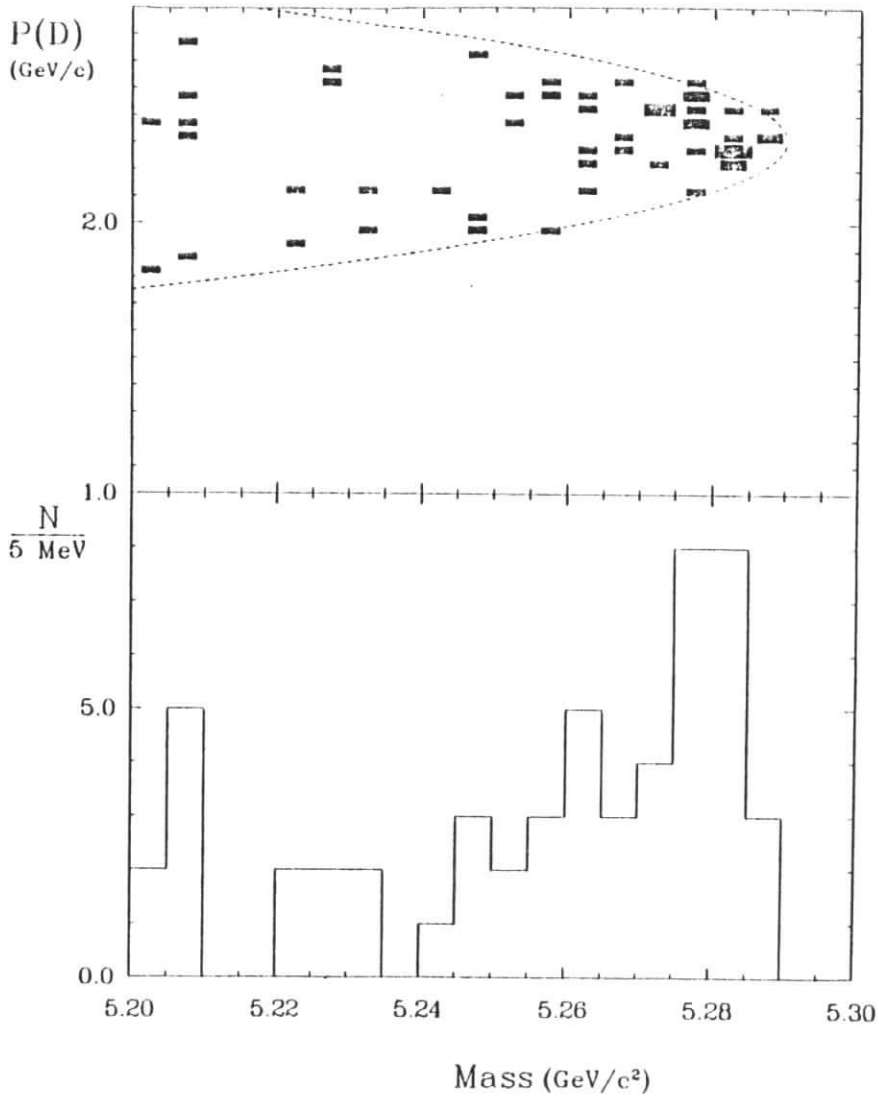

Figure 3.2: Invariant mass of $D\pi^-$ candidates: a) as a scatterplot versus D lab momentum and b) as a histogram.

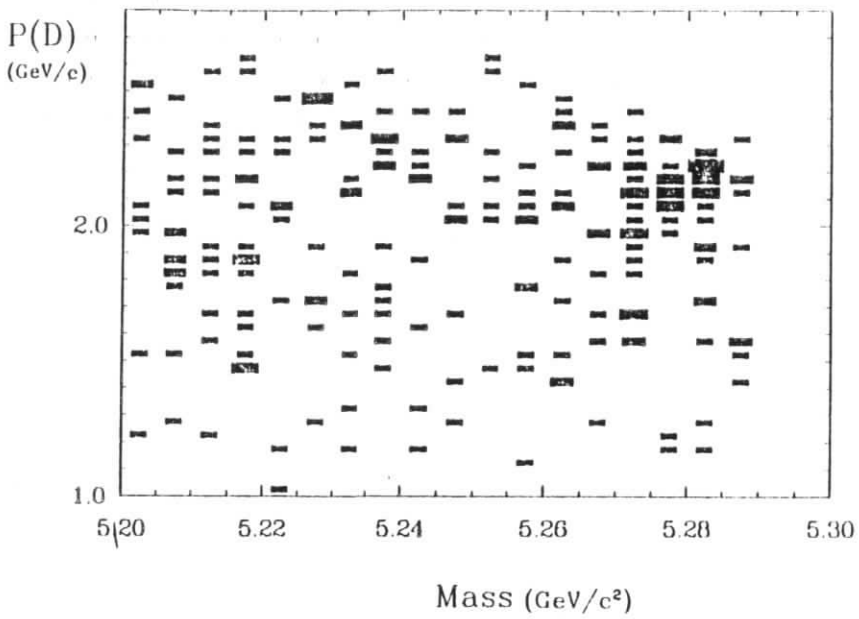

Figure 3.3: Scatterplot of the D lab momentum versus the invariant mass of the $D\pi^-\pi^0$ system.

For the decays $B^- \to D^0\pi^-\pi^0$ and $\bar{B}^0 \to D^+\pi^-\pi^0$ the results obtained using the 2 cluster π^0 candidates are presented first. Since the background is substantially larger than for the $D\pi$ candidates, the scatterplot of D momentum versus invariant mass of the system is again used to search for evidence of 2-body B decay. In Figure 3.3 a clear clustering of events is evident at D momentum of 2.2 GeV and at the B mass, a strong indication of ρ^- production. For genuine ρ events one expects a distinctive $cos^2\theta_\pi$ angular distribution characterizing a vector meson decay to two pseudoscalars in a helicity 0 state. We therefore impose the cut $|cos\theta_\pi| > 0.4$, where θ_π is the angle between one of the π's and the ρ helicity axis in the ρ rest frame. The invariant mass of the $\pi^-\pi^0$ system for B candidates in the signal region, $5.27GeV < M < 5.29GeV$, is shown in

Figure 3.4a. The invariant mass of the $D\pi^-\pi^0$ candidates with a $\pi^-\pi^0$ mass in the ρ region, $0.50GeV < M_{\pi\pi} < 1.04GeV$ or $\pm 1.75\Gamma_\rho$, is shown below in Figure 3.4b.

The signal is actually clean enough without the helicity angle cut to measure the entire helicity angle spectrum. The acceptance-corrected distribution is shown in Figure 3.5 for all candidates in the B mass and ρ mass regions defined above. The derivation of the acceptance function is discussed in Appendix C. Assuming a flat background contribution and a background level obtained from a fit procedure to be discussed in the following section, good agreement is found with a pure $cos^2\theta_\pi$ contribution for the signal.

The statistics are poor in the region $cos\theta_\pi > 0$ due to the merging of photon shower clusters from the high momentum π^0's as discussed in the selection criteria. Thus a similar analysis was performed using the single cluster π^0's. The poor energy resolution of such candidates, typically 160 MeV, required a tighter cut on the χ^2 of the B candidate energy. Rather than the usual $\chi^2 < 4$ a harsher cut of $\chi^2 < 1$ was necessary due to background considerations. Furthermore, the helicity angle was required to satisfy $cos\theta_\pi > 0.6$ to utilize the sharp $cos^2\theta_\pi$ distribution and the high acceptance near $cos\theta_\pi = 1$. The invariant mass distributions of the $\pi^-\pi^0$ system of signal B candidates is shown in Figure 3.6a while the $D\pi\pi^0$ invariant mass distribution is shown in Figure 3.6b for those events with $\pi^-\pi^0$ mass in the ρ region. In the final section of this chapter we will show that both the single- and 2-cluster samples of $\bar{B} \to D\rho^-$ decays yield quite consistent branching ratios.

The study of the decay $\bar{B} \to D\pi^-\pi^0$ is not yet complete. Having established the presence of the 2-body decays $\bar{B} \to D\rho^-$, one may search for the presence of other resonances in the final state $D\pi^-\pi^0$. Combining the distributions of the $\pi^-\pi^0$ systems from Figures 3.4a and 3.6a one obtains Figure 3.7a. The shaded histogram represents candidates from the B sideband, $5.20GeV < M < 5.26GeV$, normalized to the signal distribution for $M_{\pi\pi} > 1.85GeV$. Apart

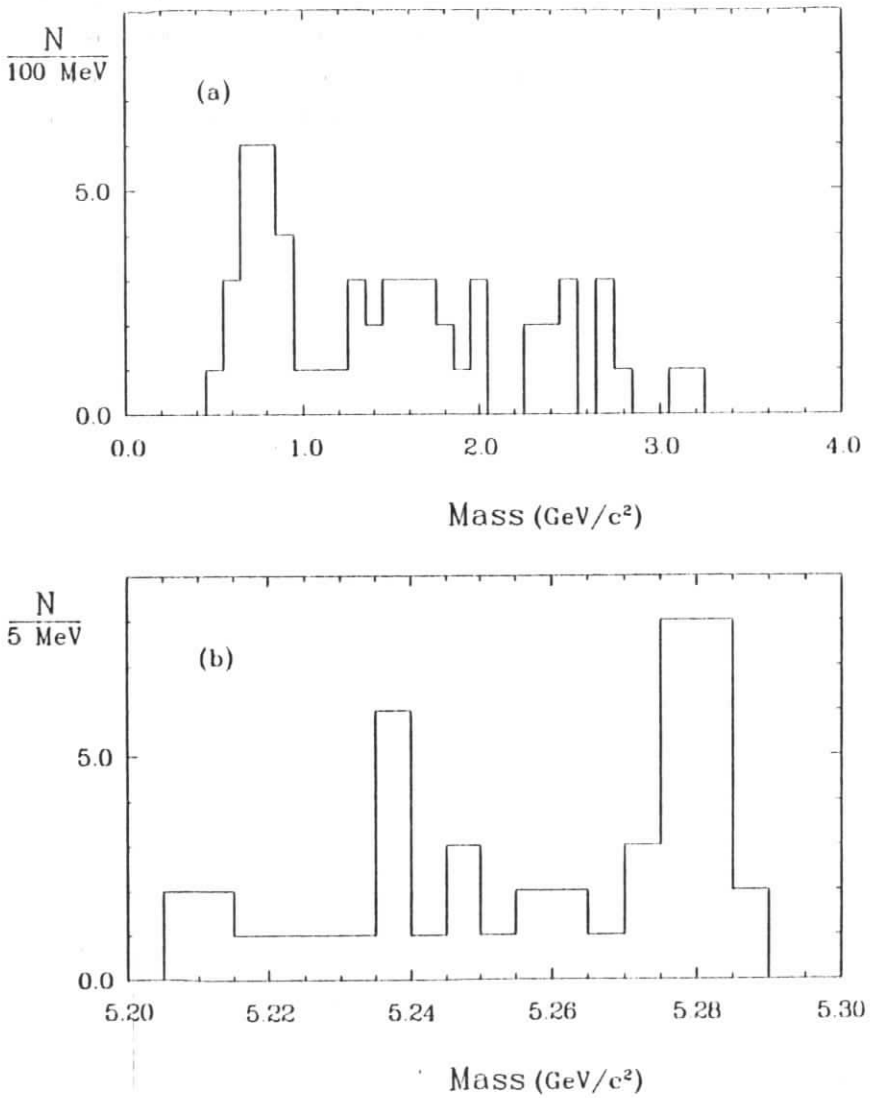

Figure 3.4: Evidence for $\bar{B} \to D\rho^-$ using the first method of π^0 reconstruction. a) Invariant mass of the $\pi^-\pi^0$ system of $\bar{B} \to D\pi^-\pi^0$ candidates and b) the invariant mass of $\bar{B} \to D\rho^-$ candidates.

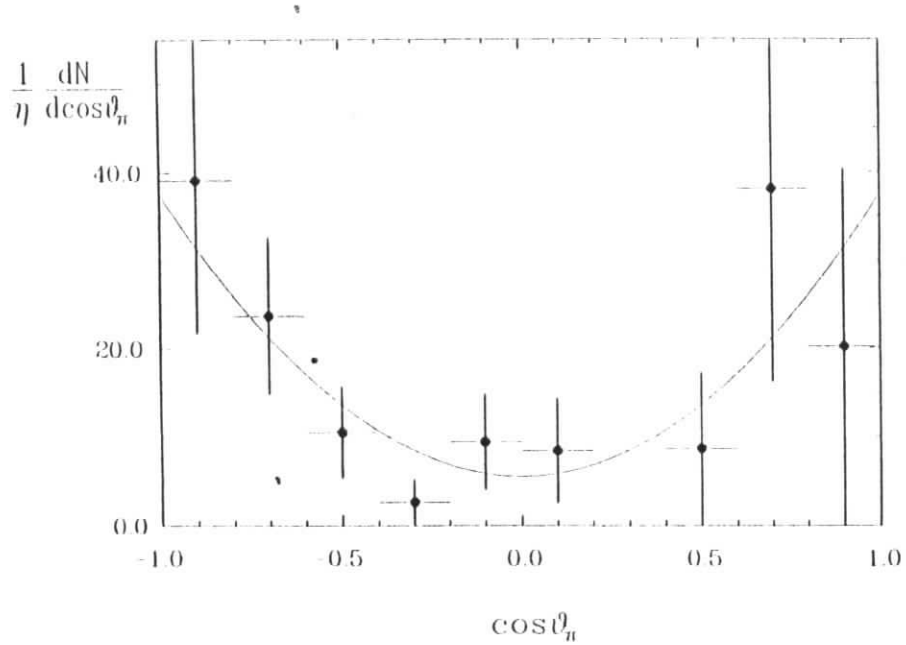

Figure 3.5: Acceptance-corrected distribution of $cos\theta_\pi$

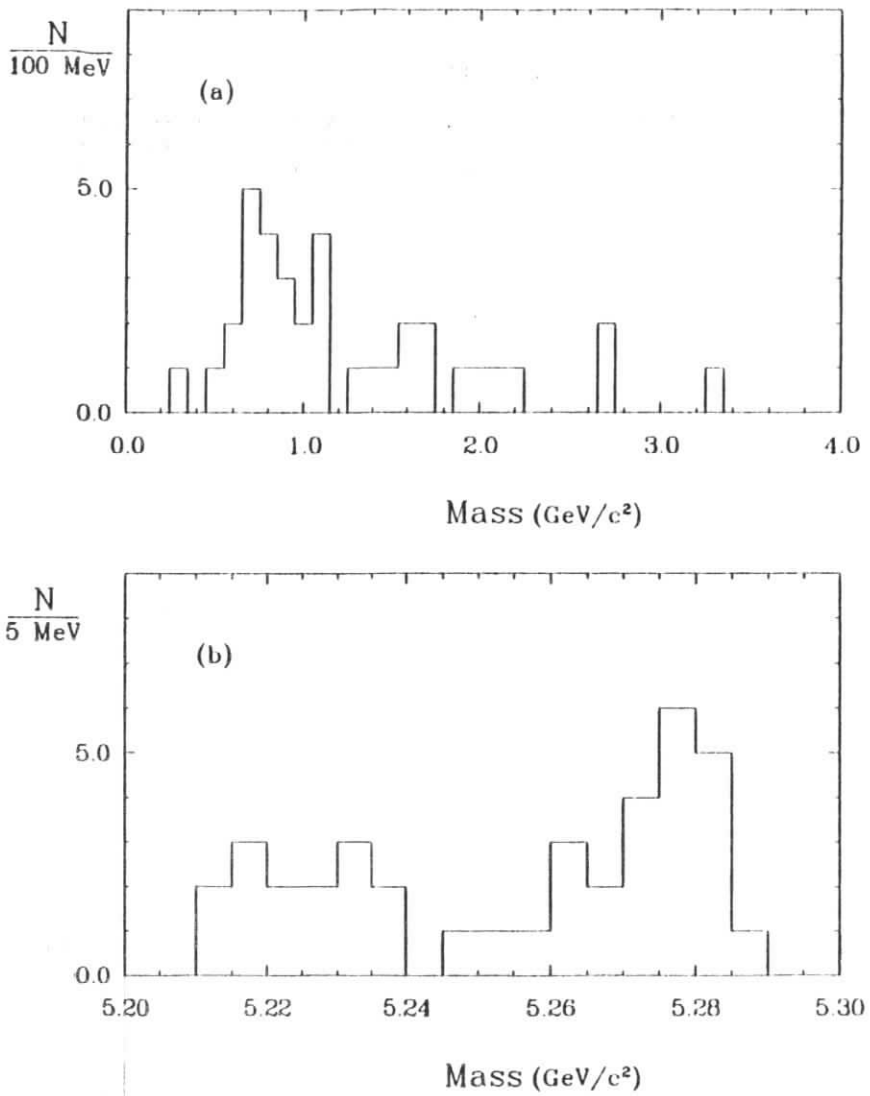

Figure 3.6: Evidence for $\bar{B} \to D\rho^-$ using the second method of π^0 reconstruction. a) Invariant mass of the $\pi^-\pi^0$ system of $\bar{B} \to D\pi^-\pi^0$ candidates and b) the invariant mass of $\bar{B} \to D\rho^-$ candidates.

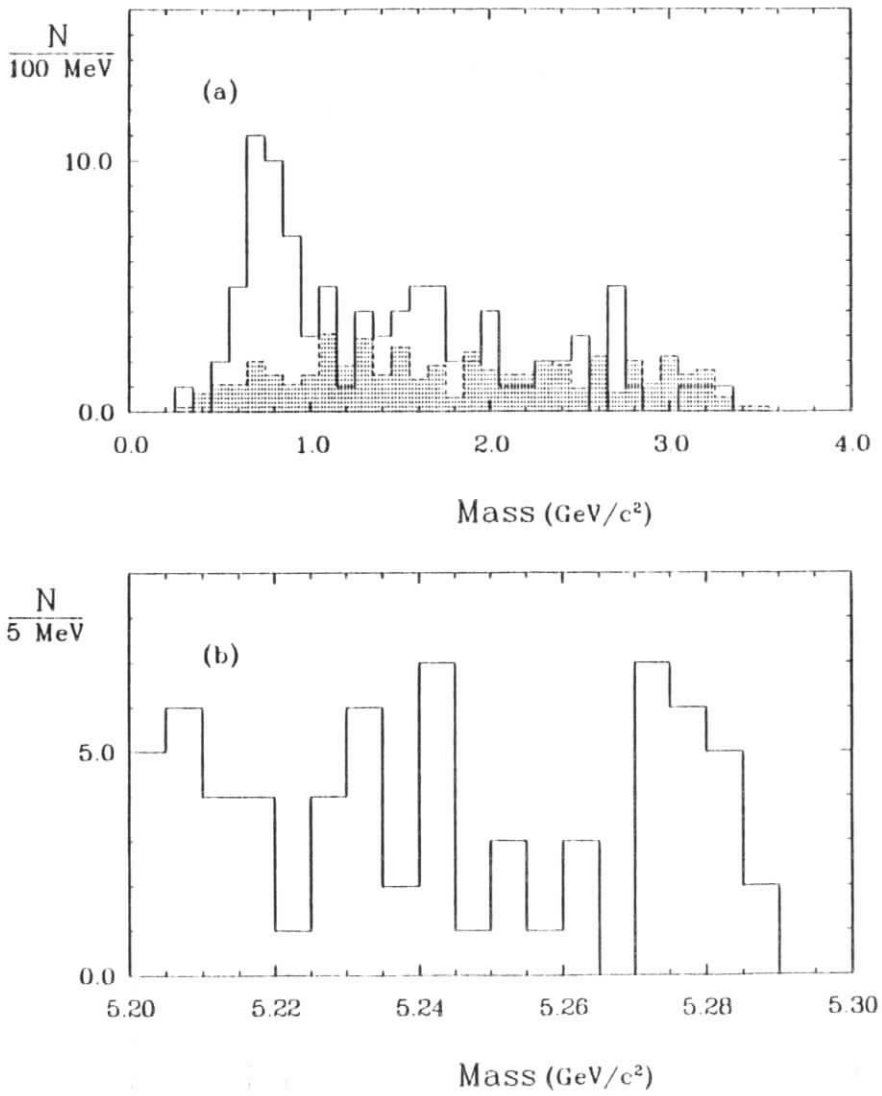

Figure 3.7: Evidence for $\bar{B} \to D^{**}\rho(1600)^-$ using both methods of π^0 reconstruction. a) Invariant mass of the $\pi^-\pi^0$ system of $\bar{B} \to D\pi^-\pi^0$ candidates and b) the invariant mass of $\bar{B} \to D^{**}\rho(1600)^-$ candidates.

from the prominant $\rho(770)$ signal some structure is evident in the mass region of $M_{\pi\pi} = 1600$ MeV consistent with previous measurements of the ρ' mass and width in the two pion mode.[1] Approximately 10 events above a comparable background level translates into more than 2 standard deviations significance. Assuming the presence of a signal, the candidates in the ρ' region, $1.33GeV < M_{\pi\pi} < 1.85GeV$, yield the B candidate mass distribution shown in Figure 7b. Again, the enhancement is nearly 2 standard deviations in excess of the background level.

The remaining $D\pi^-\pi^0$ candidates outside the ρ and ρ' regions do not show any indication of a signal. The ρ and ρ' tails may contribute as many as 5 signal events, but the background level is too high to be sensitive to this number or to a similar nonresonant $\bar{B} \to D\pi^-\pi^0$ contribution.

The decay modes $B^- \to D^+\pi^-\pi^-$ and $\bar{B}^0 \to D^0\pi^+\pi^-$ were found to have extremely large combinatorial backgrounds. Further cuts were applied to the K candidates from the D decays. To reduce particle misidentification the likelihood ratio of charged K candidates in the decays $D^+ \to K^-\pi^+\pi^+$ and $D^0 \to K^-\pi^+\pi^-\pi^+$ was required to be greater than 25%. A background from D candidates with K^0_s's which did not point back to the main vertex (indicating secondary interactions in the detector material) was suppressed by requiring that the angle β between the K^0_s momentum and the vector from the main to secondary vertex satisfy $cos\beta > 0.9$. To remove $\bar{B}^0 \to D^{*+}\pi^-$ decays from the $D^0\pi^+\pi^-$ sample, those candidates for which $|M_{D^0\pi^+} - M_{D^{*+}}| < 10MeV$ are excluded[1]. The results for both charged and neutral B decay modes are shown in Figure 3.8a.

[1] In the 1986 Particle Data Group listing of particle properties [5] the "$\rho(1600)$" resonance was listed with a branching ratio to two pions of $(23 \pm 7)\%$ and a width of 260 ± 100 MeV, each with footnotes indicating that these estimates were only educated guesses based upon several measurements, many of which quoted incompatible results. The 1988 Particle Data Group now lists two separate resonances based upon recent analyses [6].

[1] Removal of $D^{*+}\pi^-$ candidates from the $D\pi^-\pi^0$ sample is unnecessary as expected from low reconstruction efficiences of very slow π^0's.

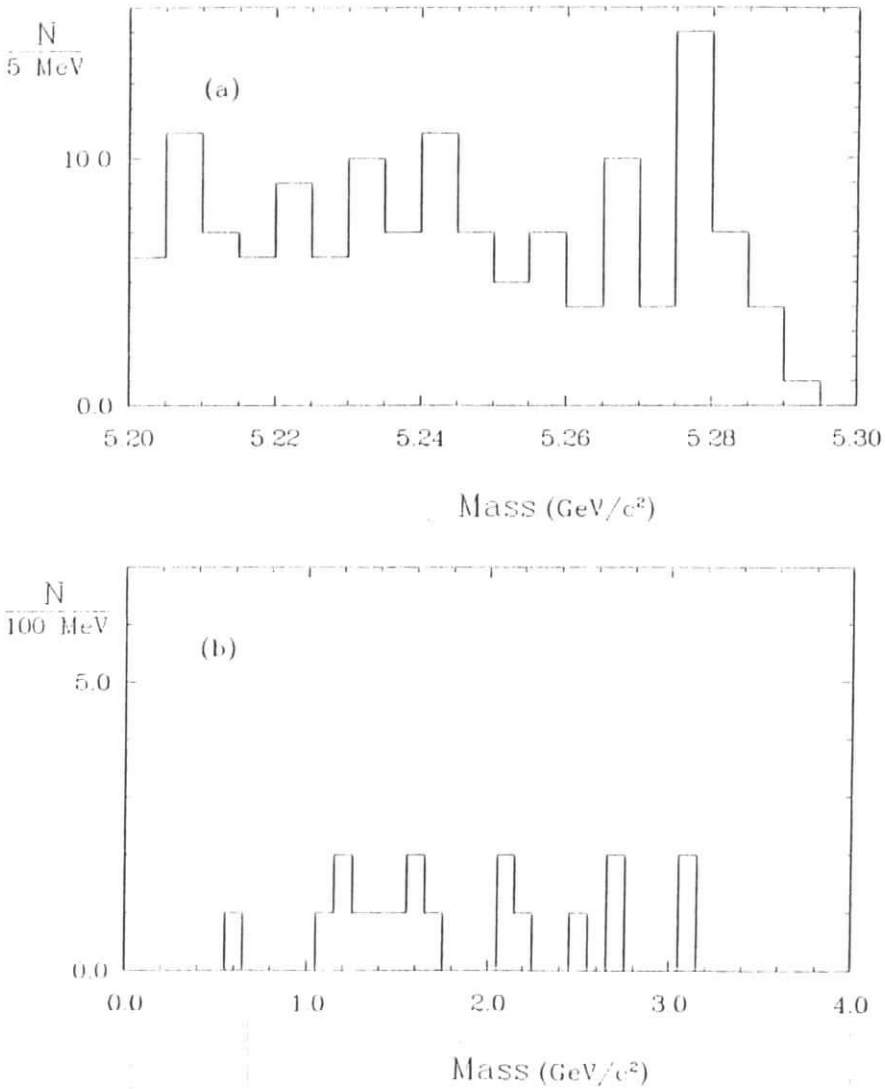

Figure 3.8: a) Invariant mass of $B^- \to D^+\pi^-\pi^-$ and $\bar{B}^0 \to D^0\pi^+\pi^-$ candidates. b) Invariant mass of $\pi^+\pi^-$ system of $D^0\pi^+\pi^-$ candidates in the B signal region.

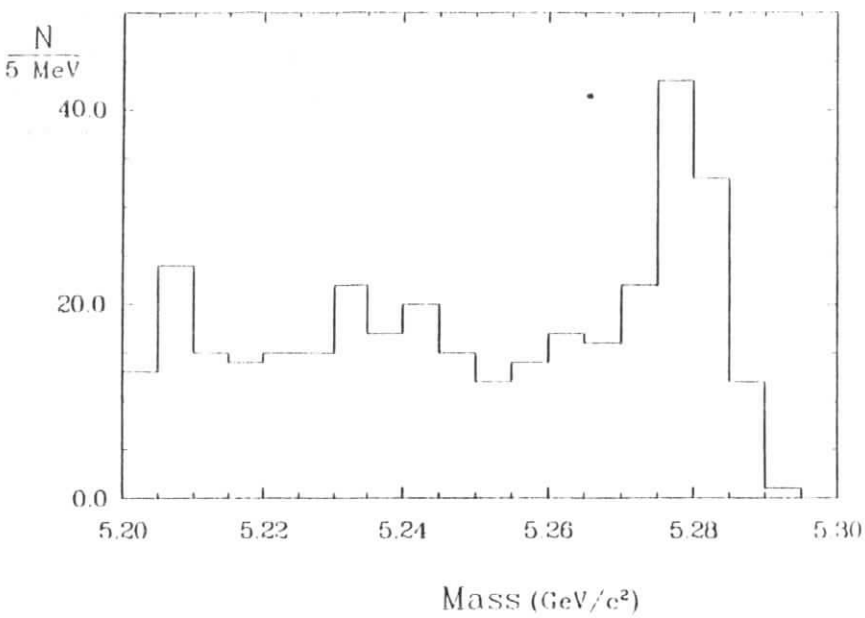

Figure 3.9: Invariant mass of all B decay modes investigated.

A search was also made for the "color-suppressed" decay $\bar{B}^0 \to D^0\rho^0$. Selecting the $D^0\pi^+\pi^-$ candidates in the B signal region yields the $\pi^+\pi^-$ distribution shown in Figure 3.8b. No evidence is seen for either a ρ or ρ' signal. No improvement is found with helicity angle cuts.

The sum of the modes $D\pi$, $D\rho$, $D\rho'$, $D^+\pi^-\pi^-$, and $D^0\pi^+\pi^-$ is shown in Figure 3.9. We find a total B signal of 61 events over a background of 49 events within the B signal region, as determined by the fits discussed in the following sections. There are 2 consistency checks which can be made on the B signal. The distribution of the angle α between thrust axes, described in the selection criteria, should be isotropic for B decays. Figure 3.10a shows this distribution for the region $0 < |cos\alpha| < 0.7$. The same distribution for the B sideband, $5.20GeV < M < 5.26GeV$, is normalized to the background level and

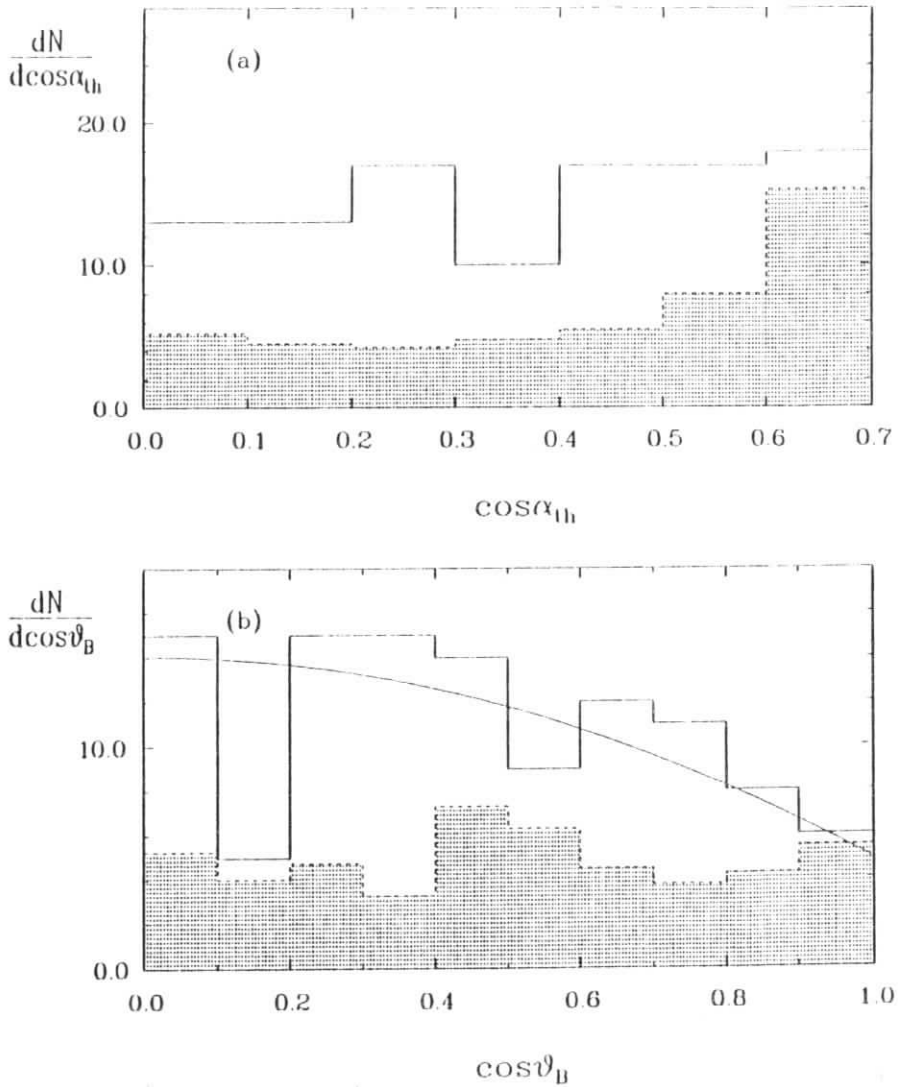

Figure 3.10: Distributions of the angle between thrust axes (a) and lab production angle of B candidates (b) for signal (open) and sideband (shaded).

is shown as a shaded histogram. The more steeply rising behavior of the sideband indicates the large percentage of continuum events in the background. The second distribution, the production angle θ_B of B candidates with respect to the beam axis, should be consistent with $sin^2\theta_B$ due to the electroweak production mechanism which yields a transversely polarized $\Upsilon(4S)$. Figure 3.10b shows this distribution for all candidates with an overlayed $sin^2\theta_B$ curve above a flat background. A χ^2 of 8 for 9 degrees of freedom is obtained.

Background studies

Determining the background level under the B signal is complicated by the threshold at $M = E_{beam}$. The objective of the background studies is to determine the shape and level of the background with reasonable certainty in order to perform the background subtraction. Emphasis is placed on the smoothness of the background shape under the B signal and the systematic uncertainties.

The background was studied using 4 separate methods: continuum data, event mixing, D-sideband combinations, and Monte Carlo. Continuum data taken at the center-of-mass energy 10.43 GeV was analysed identically to the $\Upsilon(4S)$ data except that the energy of each "B candidate" was constrained to the lower beam energy. The fitted mass is then scaled for comparison with $\Upsilon(4S)$ data by the addition of the factor $[M_{\Upsilon(4S)} - E_{cms}]/2$. Figure 3.11a shows the data for all decay modes including all cuts, scaled to the $\Upsilon(4S)$ data by the integrated luminosity ratio of $100pb^{-1}/31pb^{-1}$ and by the 1/s dependence of the continuum cross section. Continuum events account for (62 ± 11)% of all background in the B sideband, $5.20GeV < M < 5.26GeV$. Due to low statistics a background shape cannot be accurately derived, but one notes that the data do not exhibit a significant peaking at the B mass. The distribution is consistent with the shape obtained by other methods discussed below.

Event mixing was used to generate random background which simulates that

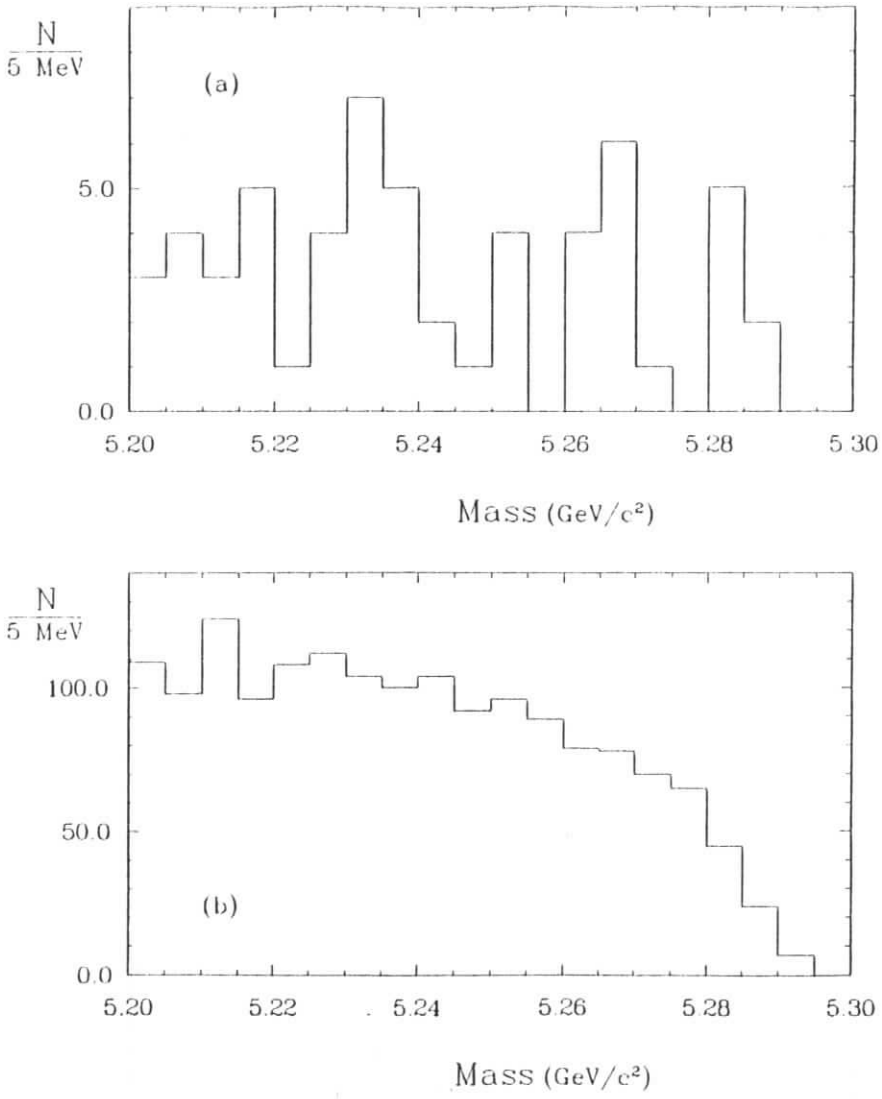

Figure 3.11: Background studies using continuum data (a) and event mixing (b).

expected from isotropic $\Upsilon(4S)$ decays. Particles from separate events are combined to form B candidates. The first method employed was to store up to 20 charged π candidates from each event into a particle buffer to be used in succeeding events in combination with $D(\pi)$ candidates. These combinations were subjected to the B selection criteria and all cuts. Likewise, D candidates were stored in buffers and combined with $\pi(\pi)$ candidates again to construct B candidates. The methods are nearly independent due to a continual replacement of buffers with particles from succeeding events during the data processing. All buffers filled from events with charged multiplicity within ± 10 of that of the current event were used for analysis. The resulting distribution is shown in Figure 3.11b for the high statistics modes $D^+\pi^-\pi^-$ and $D^0\pi^+\pi^-$. One notes the smooth behavior for such random background.

Figure 3.12a shows the D candidates used for B reconstruction. The background is roughly 20 times larger than the signal and therefore one expects fake D's to contribute the dominant part of the B background. This contribution can be estimated using D combinations from the D-sideband for "B" reconstruction. The distribution shown in Figure 3.12a represents the sum of all D candidates in the momentum interval which contributes the majority of the B candidates, $2.0GeV < P_D < 2.65GeV$, the shaded regions are the sideband and signal regions used for the analysis. The flat behavior of the D background is also observed for the interval $P_D < 2.0GeV$. Whereas signal D's are fitted to the nominal D^0 and D^+ masses [5], the sideband D's are fitted to the mass 1750 MeV with the same χ^2 cut on the mass used for signal D's. A corresponding high sideband (which would be contaminated with actual D^{*+} mesons in the $K^-\pi^+\pi^+$ mode) is not used. The resulting B candidates for all modes, represented by the open portion of the histogram in Figure 3.12b, account for $(88 \pm 9)\%$ of the background in the B sideband region. The behavior in the B signal region is reasonably smooth.

An important background source not investigated by the previous analysis involves correctly reconstructed D mesons in $\Upsilon(4S)$ events. This includes the

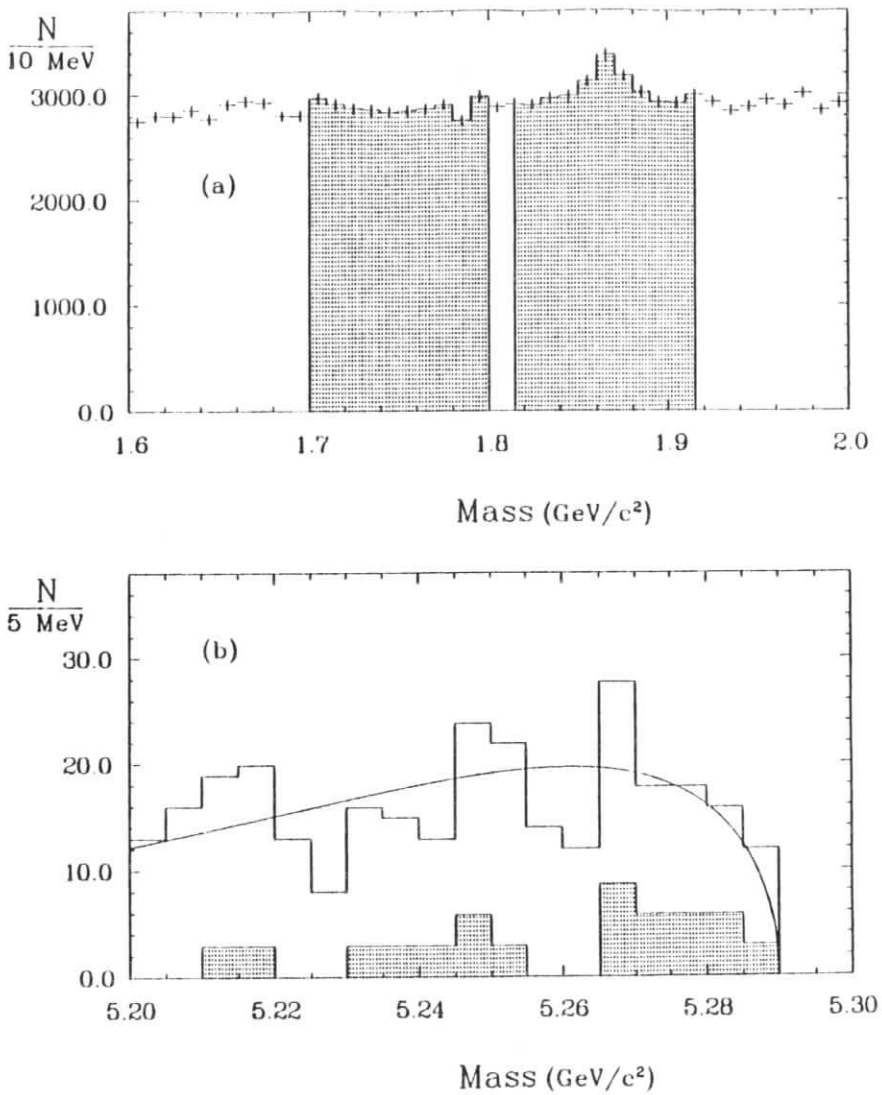

Figure 3.12: Background studies using (a) D-sideband combinations to construct B candidates (open histogram in b) for $\Upsilon(4S)$ data. The shaded portion of (b) represents Monte Carlo B background from actual D mesons.

potentially dangerous background referred to as feed-down, in which one or more slow particles from the actual B decay are neglected in the analysis. An inclusive study of this source was made using a Monte Carlo simulation of B meson decays strictly through $b \to c$ transitions. The generator used was LUND version 6.2 [24]. A realistic detector simulation was provided by SIMARG 211 [25]. Then the data was recontructed identically to actual data using version 11 of the ARGUS reconstruction program. The Monte Carlo data sample, limited by the large amount of processing time required, contains nearly 33000 $\Upsilon(4S)$ decays, corresponding to 35% of the actual $\Upsilon(4S)$ data sample. These data were analysed for B candidates with correctly reconstructed D mesons; correctly reconstructed B decay modes were excluded. This background is represented by the shaded histogram in Figure 3.12b, which has been scaled to the $\Upsilon(4S)$ data. It is evident that this source tends to populate the region near the B mass. Although it accounts for only 23 ± 8 events of the 196 events in the B sideband, it accounts for 20 ± 8 events in the B signal region. Combining this with the D-sideband analysis, (98 ± 10)% of the B sideband is accounted for. The sum of the distributions shown in Figure 3.12b appears to have a smooth behavior and is fitted with a smooth function having only two parameters:

$$F(M) = a\frac{M}{E_{beam}}\sqrt{E_{beam}^2 - M^2}\,exp[-b^2(E_{beam}^2 - M^2)] \qquad (3.1)$$

represented by the smooth curve in Figure 3.12b. The parameter a serves as normalization while b determines the shape. Though this is strictly phenomenological it does have the quality that in the limiting case of $b \to 0$ it describes a background uniformly distributed in the Lorentz invariant phase space element $\frac{P^2}{E}dP = \frac{M}{E}\sqrt{E^2 - M^2}dM$.

Although the effect of feed-down on the background shape is already accounted for in the inclusive Monte Carlo studies, additional checks were made to ensure that this background is sufficiently suppressed in the actual data. For

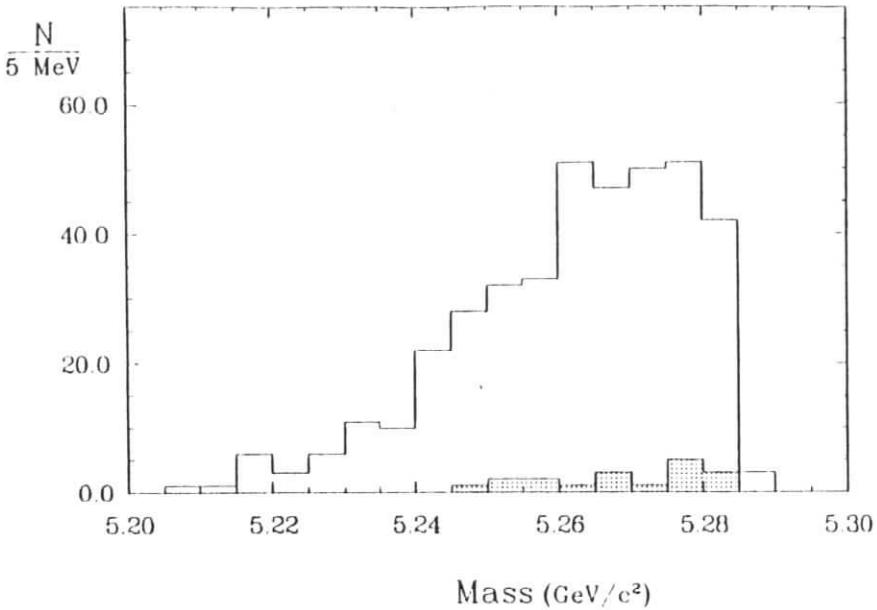

Figure 3.13: Feed-down from $\bar{B} \to D^{*0}\pi^-$ into $\bar{B} \to D^0\pi^-$ before (a) and after (b) energy cut.

example, the $D^0\pi^-$ combination from the decay chain $\bar{B}^0 \to D^{*0}\pi^-$, $D^{*0} \to D^0\pi^0$ can easily have a mass close to the B mass upon having its energy constrained to the B production energy, as shown in the Monte Carlo data of Figure 3.13. But fortunately, the χ^2 cut in the energy constraint removes nearly all of this background as indicated by the remaining amount shaded. The effect of this cut has been studied on all of the following feed-down sources:

$$\left.\begin{matrix} D^*\pi^- \\ D\rho^- \\ D, D^*l\bar{\nu} \end{matrix}\right\} \text{into } D\pi^- \text{ and } \left.\begin{matrix} D^*\rho^- \\ Da_1^- \end{matrix}\right\} \text{into } D\rho^-.$$

The amount of feed-down from $D\rho^-$ into $D\pi^-$ and Da_1^- into $D\rho^-$ in which a π^0 is neglected was found to be entirely negligible due to the substantial amount

of energy typically taken up by the missing π^0. Feed-down from D^* modes is potentially more dangerous since the mean missing energy taken up by the soft π or γ is only 210 MeV. The resolution σ_E of modes containing only charged particles in the final state is typically 30 MeV, as discussed previously; thus the energy cut at $2\sigma_E$ is quite effective in removing this source of feed-down as demonstrated in Figure 3.13. However, the situation for the $D\rho^-$ modes is worse due to the resolution of the reconstructed π^0's. Figure 3.14a shows the Monte Carlo distribution of the difference between the production energy and the measured energy of $D^0\rho^-$ candidates coming from $B^- \to D^{*0}\rho^-$ (shaded) and $B^- \to D^0\rho^-$ (open). A reasonable separation exists and feed-down is strongly suppressed by the $2\sigma_E$ cut, as shown in Figure 3.14b which agrees qualitatively with what is observed in actual data (Figure 3.14c[1]). Based on the Monte Carlo studies, the amount of feed-down in the B signal region (assuming equal $D^*\rho^-$ and $D\rho^-$ rates) is only 2 events.

As further verification that this contamination is small we note that feed-down can be further reduced by restricting the analysis to well-measured candidates which are those candidates with low π^0 momentum. Figure 3.15 shows σ_E of the $D\rho^-$ and $D\rho'^-$ candidates versus π^0 momentum in actual data. For $P_{\pi^0} < 900 MeV$ the resolution is less than 75 MeV for all candidates. Upon restricting the analysis to these candidates, the fitted $D\rho^-$ signal reduces from 16 ± 5 events to 12 ± 4 events, in good agreement with the 75% retention expected; feed-down, however, should be less than 1 event. Thus it is shown that feed-down does not enhance the signals of candidates reconstructed with two cluster π^0's, within the statistical errors.

For candidates with single cluster π^0's the situation is worse since the typical resolution of 160 MeV is not much smaller than the mean missing energy in feed-down from $\bar{B} \to D^*\rho^-$. Thus a 1 σ_E cut was applied to ensure a small feed-down rate. This suppression is strongly dependent on the helicity of the ρ^- from the

[1] Figure 3.14c represents events from both the $D\rho^-$ and $D\rho'^-$ signals.

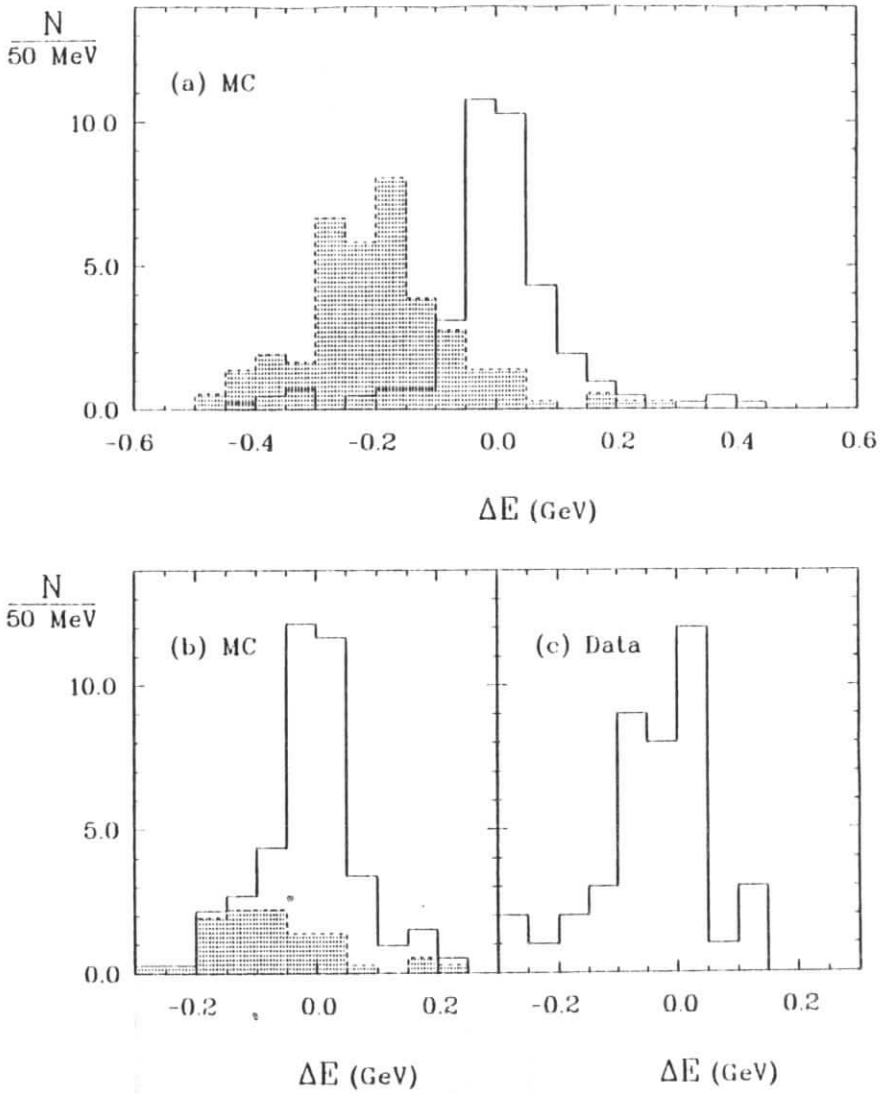

Figure 3.14: Measured energy distributions of $D^0\rho^-$ candidates from $B^- \to D^{*0}\rho^-$ feed-down (shaded) and $B^- \to D^0\rho^-$ (open) in Monte Carlo before energy cut (a) and after (b), compared with actual data (c).

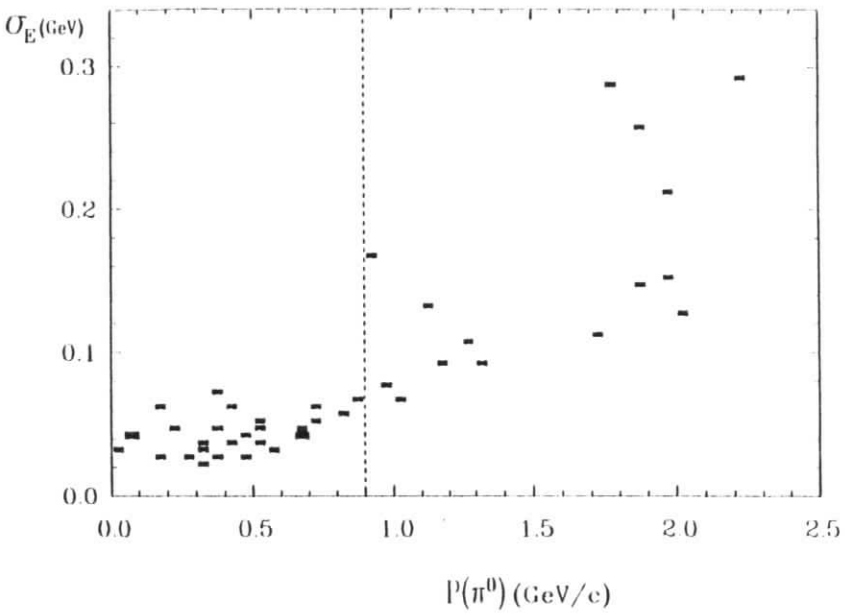

Figure 3.15: Resolution of $\bar{B} \to D\rho^-$ candidates as a function of P(π^0).

$\bar{B} \to D^*\rho^-$ decay since a large $cos^2\theta_\pi$ component will yield a sizeable fraction of single cluster π^0's. Assuming an isotropic distribution leads to the expectation of less than one event from feed-down in the data surviving the energy cut.

As a final check on feed-down from $D^*\rho^-$, the 29 D^0 candidates from the $D^0\rho^-$ and $D^0\rho'^-$ candidates in the B signal region were combined with π^+ candidates in the event to reconstruct D^{*+} candidates. Only one candidate was found to be consistent with a D^{*+} identification, i.e. within ± 10 MeV of the D^{*+} mass.

Finally, the background from semileptonic decays arising from e/π and μ/π misidentification is expected to be quite small due to the small fraction of leptons above 2.2 GeV, only 1% of the total lepton yield according to the BSW model [13]. But this background can be studied from the data itself due to the excellent lepton identification of the ARGUS detector. Of the 23 π^- candidates in the $D\pi^-$ signal none hit any muon chambers while 2 were consistent with electron identification. From the misidentification rates determined in reference [8] one would expect from a pure sample of 23 π^-'s to observe 0.6 consistent with lepton identification. Removing such candidates reduces the fitted $D\pi^-$ signal by less than one event.

In conclusion, the background level observed in the B sideband is accounted for by the background sources studied; the background shape is shown to be a smoothly varying function of the mass and the background sources which could possibly enhance the background level in the B signal region are shown to be small.

Branching ratios

The signals are obtained by fitting the mass distributions to a gaussian with a width fixed to 4 MeV and the background function of equation 3.1. The one free parameter which describes the background shape was determined by weighting

the values obtained by a maximum likelihood fit to both the background shape derived from the D-sideband and Monte Carlo studies and that observed in the actual distributions. The systematic error in the fitted signal is estimated from the difference between the signal obtained using the weighted background parameter and that using either of the parameters from the separate free fits.

There is excellent agreement between the separate fits for the $D\pi^-$ and $D\rho^-$ modes, as opposed to a possible discrepency between the separate fits to the larger background $D\rho'^-$ and $D\pi\pi$ modes, and so these are treated separately. The fit to all $D\pi^-$ and $D\rho^-$ candidates is shown in Figure 3.16a while the fit to the remaining modes is shown in Figure 3.16b. The signals and masses obtained from the fits are $N_B = 40 \pm 8$ and $M_B = (5279.7 \pm 0.9)MeV$ for Figure 3.16a and $N_B = 21 \pm 7$ and $M_B = (5278.7 \pm 1.7)MeV$ for Figure 3.16b. There is a systematic error of $3MeV$ on the masses largely due to the uncertainty in the mass of the $\Upsilon(4S)$ which sets the mass scale. Upon dividing the $D\pi^-$ and $D\rho^-$ candidates into separate B^+ and B^0 samples, the fits shown in Figure 3.17a and Figure 3.17b yield $M_{B^+} = (5278.4 \pm 1.4)MeV$ and $M_{B^0} = (5280.7 \pm 1.3)MeV$, giving a mass difference of $\Delta M_B = (2.3 \pm 1.9)MeV$, all in excellent agreement with measurements recently updated using $M_{\Upsilon(4S)} = 10580MeV$ [28,10]. The separate B^+ and B^0 masses are used to fit each signal of the individual decay modes; the sensitivity of the signals to B mass variations of order 1 MeV is negligible.

To obtain the corrected number of $D\rho^-$ and $D\rho'^-$ signals, the overlap of the Breit-Wigners must be separated. This is done by inverting the acceptance matrix in the simple equation

$$\begin{pmatrix} N_{B_1} \\ N_{B_2} \end{pmatrix} = \begin{pmatrix} \eta_{\rho\rho} & \eta_{\rho'\rho} \\ \eta_{\rho\rho'} & \eta_{\rho'\rho'} \end{pmatrix} \begin{pmatrix} N_{D\rho} \\ N_{D\rho'} \end{pmatrix} \qquad (3.2)$$

where $\eta_{\rho\rho}$ is the acceptance of ρ in the $\pm 1.75\Gamma_\rho$ mass range defining the ρ region, $\eta_{\rho'\rho}$ is the acceptance of ρ' in the same region, etc., while N_{B_1} and N_{B_2}

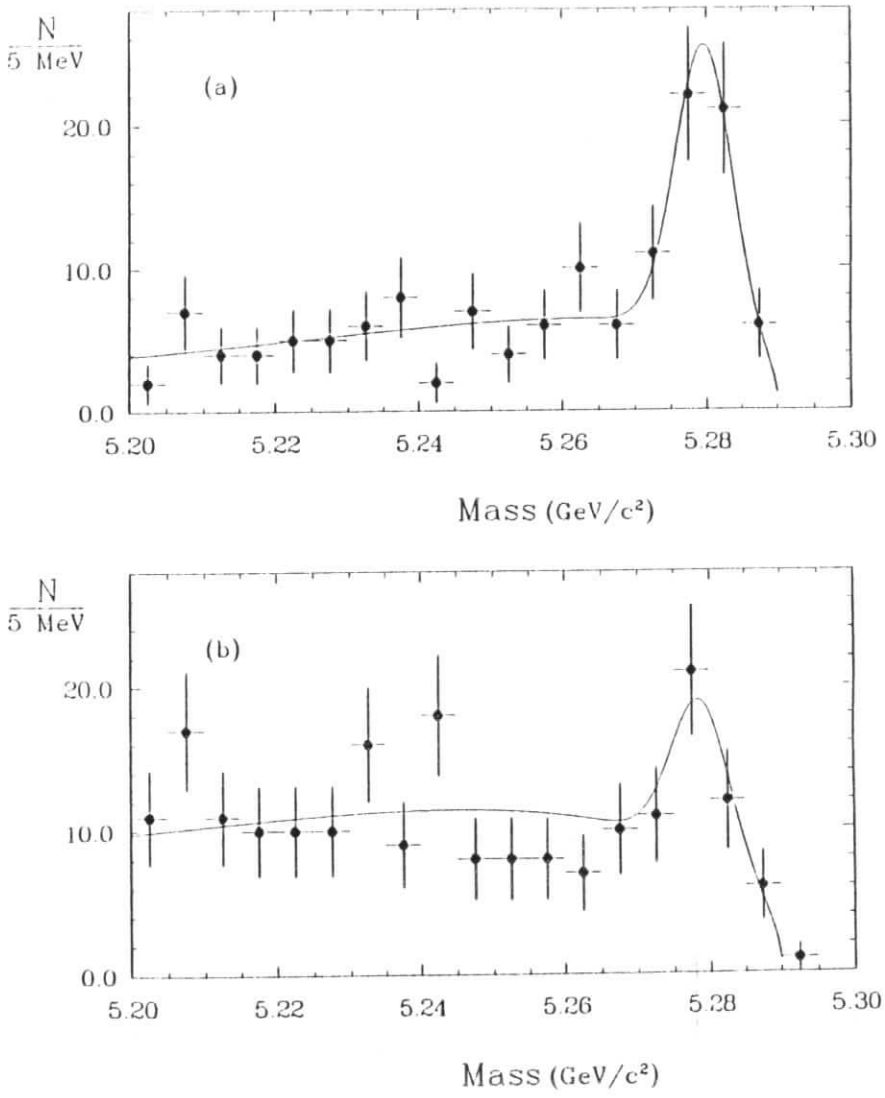

Figure 3.16: Fits to $D\pi$ and $D\rho^-$ candidates (a) and to $D\rho'^-$ and $D\pi\pi$ candidates (b).

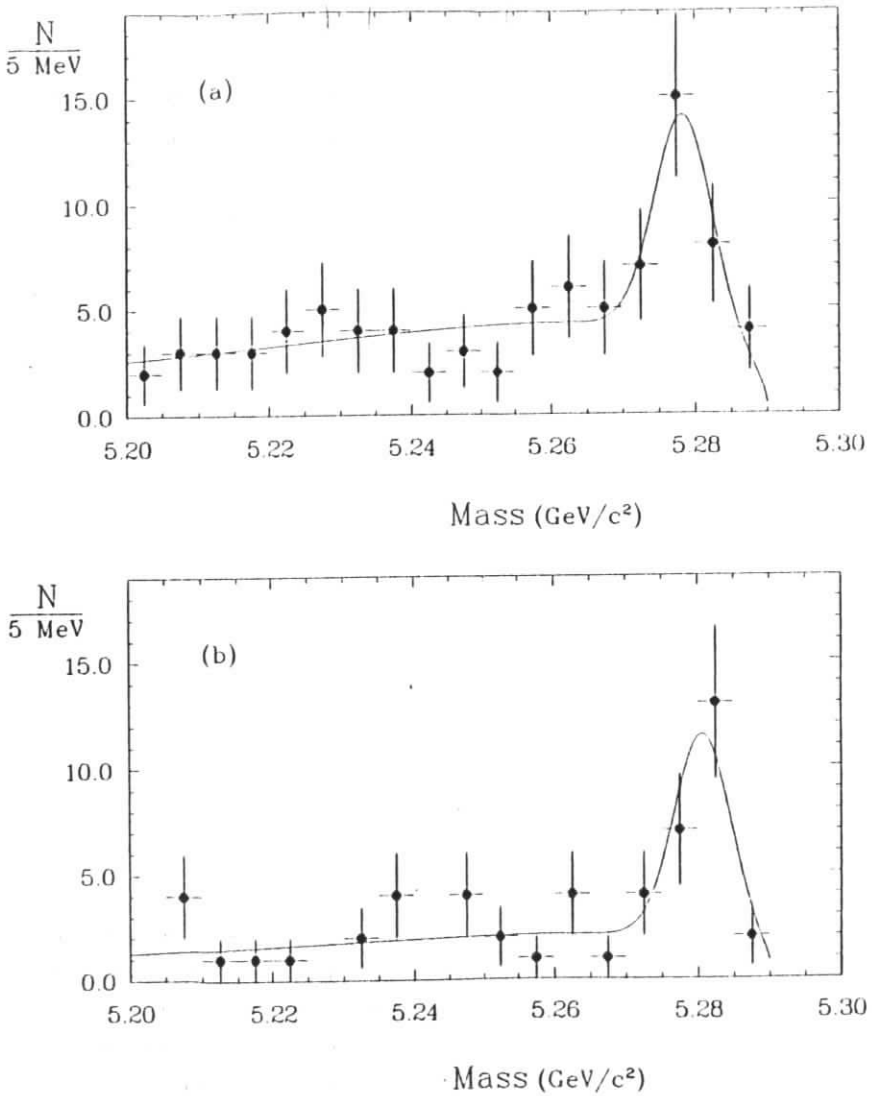

Figure 3.17: Separate fits to charged (a) and neutral (b) B candidates taken from the $D\pi^-$ and $D\rho^-$ modes only.

are the measured signals from the B mass fits to "$D\rho$" and "$D\rho'$" candidates respectively. Two non-interfering Breit-Wigners of the form $\Gamma = \Gamma_0(\frac{q}{q_0})^{2l+1}\frac{E_0}{E}$ [26] are used where q and E are the momentum and energy of each π in the rest frame of the decaying ρ and q_0, E_0 are the corresponding values for decays from the central value of the resonance. Variations of the ρ' parameters have a negligible effect on the fitted ρ signal, whereas large uncertainties in the ρ' signal arise from possible interference effects with the ρ tail and uncertainties in the ρ' width (See reference [6]). The acceptance matrix is

$$\eta = \begin{pmatrix} 0.85 & 0.02 \\ 0.04 & 0.75 \end{pmatrix}$$

The only non-negligible overlap is 1 event from the ρ signal in the ρ' region of $\pm 1\Gamma_{\rho'}$. The resulting signals are 29 ± 7 $D\rho$ events and 10 ± 6 $D\rho'$ events. As a cross check on these numbers the $\pi^-\pi^0$ mass spectrum was fitted using a second order polynomial with square root constraints at each kinematic threshold for the background shape. The fit, shown in Figure 3.18, yields 31 ± 9 events for the ρ signal and 11 ± 8 for the ρ' signal.

The reconstruction efficiencies were derived from Monte Carlo studies. Events were generated using LUND version 6.2 [24] and put through the ARGUS detector simulation [25], then reconstructed and analysed as for actual data. A matching of reconstructed events with the generated events is done to obtain the acceptances. The procedure of selecting the candidate with the maximum probability required only a small correction for the $D\rho$ and $D\rho'$ modes as discussed in Appendix B. The D^0 and D^+ reconstruction efficiencies for the 2-body $D\pi$ and $D\rho$ decay modes are $(6.0 \pm 0.6)\%$ for D^0 and $(4.5 \pm 0.6)\%$ for D^+ and slightly smaller for the $D\rho'$ and $D\pi\pi$ modes. The errors are dominated by the systematic uncertainties in the D decay branching ratios [21]. For the $D\pi\pi$ modes the Monte Carlo events were generated according to 3-body phase space, which appears to behave very similar to the candidates in the data. The Monte

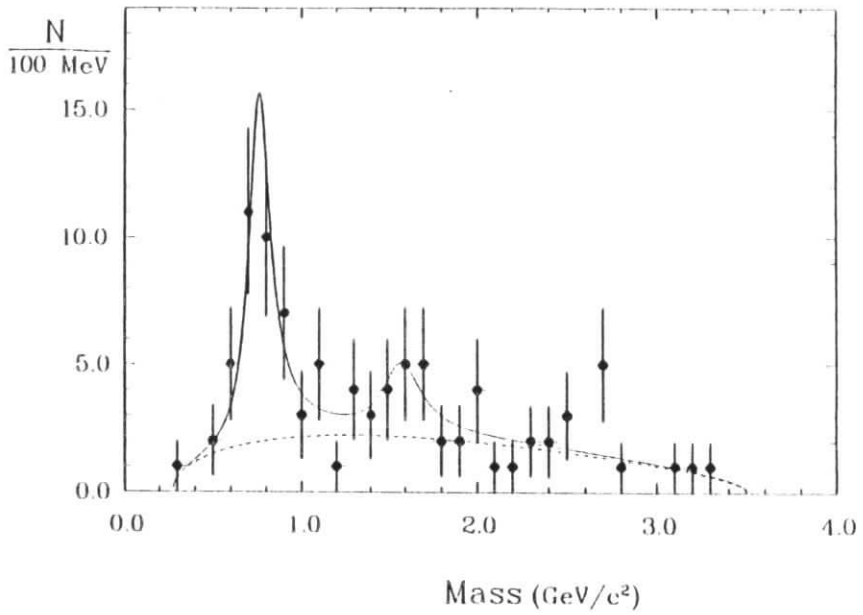

Figure 3.18: Fit to $\pi^0\pi^-$ invariant mass spectrum

Carlo π^0 acceptance was compared with the acceptance of π^0's from the clean reaction $\gamma\gamma \to \pi^+\pi^-\pi^0$; no significant differences are observed and a conservative 10% systematic uncertainty is attributed to the $D\rho$ and $D\rho'$ reconstruction efficiencies obtained from the Monte Carlo π^0 acceptance.

The major component of systematic uncertainty in the branching ratios is from the background determination, conservatively given as 25% for the $D\pi$ and $D\rho$ modes and 40% for the $D\rho'$ and $D\pi\pi$ modes. As mentioned previously, the ρ' parameters and decay branching ratios are very uncertain; we take the values given in reference [5] as rough estimates. Though uncertainties in the ρ' parameters are not included in the systematic errors, the $D\rho'$ modes contain a 30% uncertainty from the $\rho'^- \to \pi^-\pi^0$ branching ratio. Table 3.1 lists the B signals, the background within $5.27GeV < M < 5.29GeV$ or $\pm 2.5\sigma$ of the B mass, the reconstruction efficiencies, and the branching ratios with statistical and systematic errors.

The separate π^0 reconstruction methods for $B^- \to D^0\rho^-$ yield the branching ratios $(1.9 \pm 0.8)\%$ for the two cluster π^0's and $(2.3 \pm 1.1)\%$ for the single cluster π^0's, while for $\bar{B}^0 \to D^+\rho^-$ the branching ratios are $(2.9 \pm 1.2)\%$ and $(2.5 \pm 1.5)\%$ for the respective methods. The branching ratios of the separate methods are quite consistent for both decay modes. Only the weighted average of the two methods are given in Table 3.1 for the $D\rho$ and $D\rho'$ modes. For these modes the background listed is within the cuts on the ρ and ρ' regions, namely $\pm 1.75\Gamma_\rho$ and $\pm 1\Gamma_{\rho'}$. For the modes $D^0\rho^0$ and $D^0\rho'^0$, where no signals are observed, all events in the B signal region and the ρ and ρ' regions respectively are considered signal events, while the upper limits given are Poisson 90% confidence level limits.

Decay mode	Signal	Background	Efficiency	Branching Ratio (%)
$B^- \to D^0 \pi^-$	7	6 ± 3	0.036	$0.19 \pm 0.10 \pm 0.06$
$\to D^0 \rho^-$	16	7 ± 3	0.0080	$2.0 \pm 0.7 \pm 0.7$
$\to D^0 \rho'^-$	5	4 ± 2	0.0016	$^*3.1 \pm 2.7 \pm 1.8$
$\to D^+ \pi^- \pi^-$	7	5 ± 3	0.015	$0.46 \pm 0.22 \pm 0.22$
$\bar{B}^0 \to D^+ \pi^-$	8	2 ± 1	0.027	$0.35 \pm 0.14 \pm 0.12$
$\to D^+ \rho^-$	13	5 ± 3	0.0057	$2.7 \pm 1.0 \pm 1.0$
$\to D^+ \rho'^-$	5	8 ± 3	0.0014	$^*4.3 \pm 3.7 \pm 2.5$
$\to D^0 \pi^- \pi^+$	5	13 ± 4	0.021	$0.28 \pm 0.24 \pm 0.13$ < 0.7 at 90% CL
$\to D^0 \rho^0$	< 4		0.017	< 0.3 at 90% CL
$\to D^0 \rho'^0$	< 9		0.0035	$^*< 3$ at 90% CL

*using the ρ' mass, width, and branching ratios given in reference [5]

Table 3.1: Branching ratios of exclusive decays investigated

Chapter 4

Discussion and Conclusion

Comparisons with theoretical predictions

The measurements are now compared with other existing measurements of exclusive B decays to charmed mesons [27-32] and with the predictions of various models [12,14,16]. All measured branching ratios together with available predictions are listed in Table 4.1. The ARGUS and CLEO measurements were made using similar analyses. All measurements are updated using the D decay branching ratios of reference [21] and the $D^{*+} \to D^0 \pi^+$ branching ratio of reference [22]. ARGUS assumes the ratio of neutral to charged B mesons produced in $\Upsilon(4S)$ decays to be 45:55 while CLEO assumes the ratio to be 43:57. The model of Hussain and Scadron [14] is abbreviated HS and the Bauer, Stech, and Wirbel model [12] is abbreviated BSW. The Körner model [16] is a slight modification of an earlier work by Ali, Körner, and Kramer [15].

All three models are actually fairly similar as mentioned in the introduction, each based upon a simple spectator decay process and assuming factorization in the hadronization to mesons. For the coefficients in the effective hamiltonian (see equation 1.2 and the following discussion) Körner and BSW use only the leading term in a $1/N_c$ expansion, i.e. no color suppressed contributions, whereas HS ignore the neutral current factor c_2 and argue for a relative negative sign between leading and color suppressed contributions. Both approaches yield

Decay mode	ARGUS	CLEO	HS	Körner	BSW
B^- modes					
$D^0\pi^-$	$0.19 \pm 0.10 \pm 0.06$	$0.47^{+0.16+0.11}_{-0.13-0.08}$	0.16	0.35	0.4
$D^0\rho^-$	$2.0 \pm 0.7 \pm 0.7$		0.71	0.73	1.3
$D^{*0}\pi^-$		0.27 ± 0.44	0.47	0.14	0.3
$D^+\pi^-\pi^-$	$0.46 \pm 0.22 \pm 0.22$	$0.25^{+0.41+0.24}_{-0.23-0.08}$			
$D^{*+}\pi^-\pi^-$	$0.5 \pm 0.2 \pm 0.3$	$0.21^{+0.15+0.08}_{-0.14-0.05}$			
$D^{*+}\pi^-\pi^-\pi^0$	$4.7 \pm 1.4 \pm 2.9$				
$J/\psi K^-$	0.07 ± 0.04	0.05 ± 0.02		0.05	0.06
¶$J/\psi K^-\pi^+\pi^-$	0.11 ± 0.07				
$\psi' K^-$	0.22 ± 0.17				
$\bar{B}^0$ modes					
$D^+\pi^-$	$0.35 \pm 0.14 \pm 0.12$	$0.59^{+0.33+0.15}_{-0.29-0.14}$	0.36	0.55	0.6
$D^+\rho^-$	$2.7 \pm 1.0 \pm 1.0$		0.64	1.27	1.5
$D^{*+}\pi^-$	$0.30 \pm 0.15 \pm 0.11$	$0.46 \pm 0.12 \pm 0.10$	0.33	0.47	0.5
$D^{*+}\pi^-\pi^0$	$1.7 \pm 0.9 \pm 0.9$		†0.73	†1.0	†1.5
$D^{*+}\pi^-\pi^+\pi^-$	$3.6 \pm 1.0 \pm 1.8$	$2.6 \pm 0.9 \pm 1.1$			†1.9
§$D^0\pi^-\pi^+$	< 0.7	< 3.9			
$D^0\rho^0$	< 0.3				0.004
$D^+D_s^-$		1.1 ± 1.0	1.00	0.95	0.8
$D^{*+}D_s^-$	$1.1^{+1.7}_{-1.3} \pm 0.4$		0.33	0.67	0.4
$D^{*+}D_s^{*-}$	$5^{+3}_{-2} \pm 1$		2.93	5.6	2.4
$D^{*+}l^-\bar{\nu}$	$7.0 \pm 1.2 \pm 1.9$				
$J/\psi K^0$		0.04 ± 0.03		0.10	0.06
$J/\psi K^{*0}$	0.33 ± 0.18	0.06 ± 0.03		0.23	0.25

¶Not $\psi' K^-$ §Not $D^{*+}\pi^-$ †Only $D^{*+}\rho^-$ †Only $D^{*+}a_1^-$

Table 4.1: Experimental and theoretical branching ratios for exclusive B meson decays to charmed mesons

nearly the same effect on the predicted rates, which is not surprising since the authors were motivated to describe the existing D decay data reasonably well. For the parameters necessary for the calculation of branching ratios, namely the KM matrix element $|V_{bc}|$ and the B meson lifetime τ_B, the authors differ slightly. The authors HS, Körner, and BSW use the values $|V_{bc}| = 0.06, 0.045, 0.05$ respectively and $\tau_B = 1.2, 1.27, 1.2$ in units of 10^{-12} seconds respectively. Each author assumes equal lifetimes for charged and neutral B mesons.

We begin the comparisons by noting that the measured branching ratios of $\bar{B} \to D\rho^-$ relative to those of $\bar{B} \to D\pi^-$ are quite large, although not in disagreement with the predicted enhancements which vary from 2 to 4. We also note that the upper limit on the branching ratio of the decay, $\bar{B}^0 \to D^0\rho^0$, is one order of magnitude lower than the branching ratios of the $D\rho^-$ modes, a strong indication that the contribution from the "color suppressed" diagram (e.g. Figure 1.3b) is indeed small. This is consistent with the BSW predictions.

The existence of "color suppressed" diagrams is supported by B decays to charmonium, which proceed via $b \to c\bar{c}s$. However, the branching ratios of these decays are one order of magnitude lower than the decays involving D_s^-, which are also expected to occur dominantly via $b \to c\bar{c}s$ but through the nonsuppressed diagram involving independent W^- fragmentation. These measurements are consistent with all of the available predictions for decays to J/ψ and D_s^-.

A further test of the theoretical treatment of these diagrams is whether or not the Pauli-suppression (destructive interference between the two diagrams) can be observed in B decays. Assuming equal charged and neutral B lifetimes, we compare the branching ratios of the charged and neutral B decays to $D\pi^-$ and $D\rho^-$. Although the branching ratios of $B^- \to D^0\pi^-$ and $\bar{B}^0 \to D^+\pi^-$ are consistent with being equal within the errors, also true of $B^- \to D^0\rho^-$ and $\bar{B}^0 \to D^+\rho^-$, the measurements favor slight suppressions in the B^- decays relative to the $\bar{B}^0$ decays, in agreement with most of the relevant predictions.

Next we focus our attention on the available measurements for the corresponding modes involving D and D^* mesons. We see from Table 4.1 that the branching ratios of exclusive B decays to D mesons are consistently very similar to corresponding B decays to D^* mesons as is generally predicted. This may be understood on the basis of the $V-A$ weak interaction in inclusive B decays to D and D^* mesons, which we discuss next.

Relation to inclusive $\bar{B} \to D + X$ measurements

Since the measurements of inclusive D production in B decays have substantially smaller statistical errors than exclusive B decay measurements, the precision of exclusive D decay branching ratios are quite important here. We use once again the branching ratios of $D^0 \to K^-\pi^+$ and of $D^+ \to K^-\pi^+\pi^+$ from reference [21] and that of $D^{*+} \to D^0\pi^+$ from reference [22]. The results of the two available measurements [33,34] of the inclusive decays of B mesons to D^0, D^+, and D^{*+} mesons are averaged to obtain the branching ratios:

$$\begin{aligned} BR[\bar{B} \to D^0 + X] &= (48.3 \pm 4.7 \pm 6.5)\% \\ BR[\bar{B} \to D^+ + X] &= (21.9 \pm 3.6 \pm 3.3)\% \\ BR[\bar{B} \to D^{*+} + X] &= (30.0 \pm 3.8 \pm 5.0)\%. \end{aligned}$$

The first error is the statistical and systematic errors of the inclusive D measurements taken in quadrature while the second is the error in the D decay branching ratios. Note that the three categories are not mutually exclusive; the D^{*+} decays contribute to the D^0 and D^+ channels.

We define D mesons from B decays which are not decay products of D^* mesons as "direct" D's. Since the spectator model appears to describe B decays reasonably well, we may assume the following relationship:

$$\frac{BR(\bar{B} \to D^{*+}_{dir} + X)}{BR(\bar{B} \to D^{+}_{dir} + X)} = \frac{BR(\bar{B} \to D^{*0}_{dir} + X)}{BR(\bar{B} \to D^{0}_{dir} + X)}.$$

Using this and the branching ratio $BR(D^{*+} \to D^0\pi^+) = (57 \pm 10)\%$ [22] one finds:

$$\begin{aligned} BR[\bar{B} \to D^0_{dir} + X] &= (7 \pm 4)\% \\ BR[\bar{B} \to D^+_{dir} + X] &= (9 \pm 6)\% \\ BR[\bar{B} \to D^{*0}_{dir} + X] &= (24 \pm 7)\% \\ BR[\bar{B} \to D^{*+}_{dir} + X] &= (30 \pm 6)\%. \end{aligned}$$

The 3:1 enhancement of D^* production over direct D production in inclusive B decays happens to coincide with the respective number of spin degrees of freedom. This ratio can be understood qualitatively from dynamical effects of the $V-A$ weak interaction. If the W^- couples to a lepton-antineutrino pair rather than a quark-antiquark pair, the decay process simplifies somewhat the effects of strong interactions. For low q^2 values of the off-shell W^-, the momentum of the W^- system is large in the rest frame of the massive b quark, and the momenta of the $l^-\bar{\nu}$ pair will be nearly parallel as visualized in Figure 4.1a. The weak interaction strongly favors left-handed light fermions and right-handed light antifermions, thus a net 0 helicity system. This results in the production of both D and D^* mesons in the $c\bar{q}$ system at low q^2 values. Furthermore, since the D and D^* spatial wave functions are expected to be very similar and extra phase space suppression of the only slightly more massive D^* is very small, we expect their rates to be very similar in this limit. But at the high q^2 limit the $l^-\bar{\nu}$ pair has a large opening angle, favoring alligned spins as shown in Figure 4.1b. Helicity conservation requires a spin flip in the b-quark transition to a c-quark, thus resulting in a $\bar{B} \to D^*$ transition.

A prediction [17] for the direct D and D^* rates as functions of q^2 (which agrees nicely with the recent ARGUS measurement [35] of the decay $\bar{B}^0 \to D^{*+}l^-\bar{\nu}$) is shown in Figure 4.2. The D and D^* rates are nearly identical at low q^2 but the D rate falls off rapidly with increasing q^2 whereas the D^* rate is enhanced, in agreement with the above description. The overall large enhancement of D^* mesons in B decays is then explained by the large range of q^2 values available

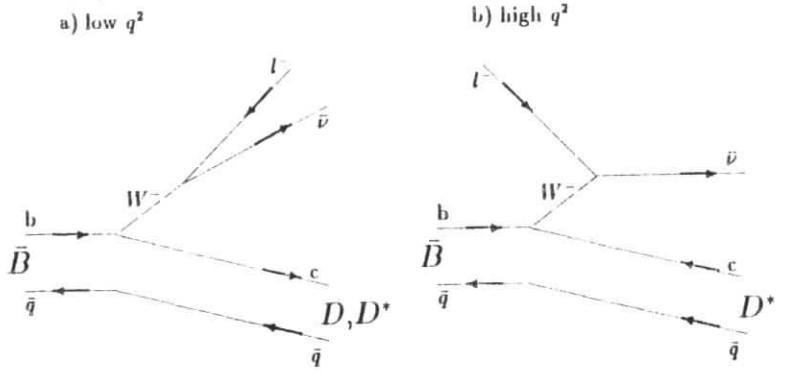

Figure 4.1: Diagrams showing helicity structure in the decay $\bar{B} \to D(D^*)l^-\bar{\nu}$

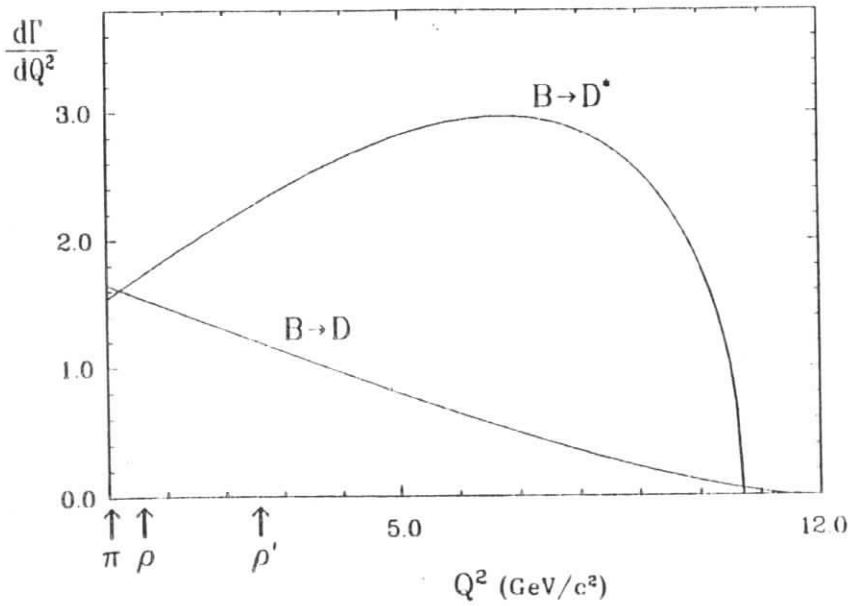

Figure 4.2: Decay widths of $\bar{B} \to D, D^* + l^-\bar{\nu}$ as functions of q^2 [17]

in B decays. For this model of semileptonic B decays an overall enhancement of 3:1 in the relative rates of D^* and D is predicted. This is to be compared with semileptonic D decays for which K^* production is expected to be nearly equal to direct K production since the q^2 range is much smaller in D decays [13,17]. However, recent measurements indicate that K^* production may be even less than direct K production in both semileptonic D decays [36,37] and in inclusive D decays [38]. Nonetheless, it is clear that the dynamical effects of the $V-A$ weak interaction are quite important in the ratio of vector to pseudoscalar production.

Returning to the hadronic decays, the same dynamical effects that occur in the semileptonic decays apply if the W^- couples to the light $\bar{u}d$ quark pair. As discussed in the previous section, strong effects appear to be quite small beyond the binding within the hadrons. Though the q^2 dependence shown in Figure 4.2 would be modified, particularly at low q^2 where hadronic resonances such as π^-, ρ^-, or ρ'^- lie, the relative rates of D and D^* production should be very similar to that of semileptonic decays. Since the 2-body hadronic decays occur at low q^2, where D and D^* production rates should be nearly equal, we see that the similar rates observed for corresponding D and D^* modes are consistent with the large enhancement of D^* production in inclusive B decays.

Conclusion

The decays $\bar{B} \to D\rho^-$ are observed for the first time in data taken by the ARGUS detector. The measured branching ratios of the decays $B^- \to D^0\rho^-$ and $\bar{B}^0 \to D^+\rho^-$ are $(2.0 \pm 0.7 \pm 0.7)\%$ and $(2.7 \pm 1.0 \pm 1.0)\%$ respectively. These are substantially larger than those of the decays $\bar{B} \to D\pi^-$ or that of the "color suppressed" decay $\bar{B}^0 \to D^0\rho^0$. Suggestive, yet inconclusive evidence is found for the existence of the decays $\bar{B} \to D^*\rho(1600)^-$. All measurements of the decays $\bar{B} \to D\pi, D\pi\pi$ appear to be consistent with other available measurements

of exclusive B decays and with theoretical predictions based upon a spectator decay model. Similar branching ratios for corresponding decays with D^* mesons can be reconciled with the large enhancement of D^* production relative to direct D production in inclusive B decays through the dynamical effects of the $V-A$ weak interaction.

Appendix A

Resolution of B signal

Since B mesons produced by the decay of the $\Upsilon(4S)$ at rest in the lab are also nearly at rest ($\beta \approx 0.06$) in the lab, the reconstructed B mass resolution is dominated by the measured energy resolution, $\sigma_M \approx \sigma_E$, which varies from typically 30 MeV for decay modes yielding only charged final state particles to typically 160 MeV for decay modes involving high momentum photons. The energy constraint, $E_B = E_{beam}$, removes the error due to the energy measurement and improves the measured momentum resolution. For the charged modes the error in the momentum σ_P improves modestly from 20 MeV to 15 MeV whereas for the modes with high momentum photons the improvement is dramatic, from 120 MeV to 25 MeV. Thus, excluding the uncertainty due to the spread in the beam energy, one expects a mass resolution of $\sigma_M = \gamma\beta\sigma_P = 0.9$ MeV for the charged modes and 1.5 MeV at worst.

Taking into account the spread in the DORIS II beam energy of slighty more than 6 MeV one obtains a center-of-mass energy resolution of ≈ 9 MeV. This is improved by the narrow shape of the relativistic $\Upsilon(4S)$ Breit-Wigner which has a natural width of (24 ± 2) MeV [5]. The probability of producing the $\Upsilon(4S)$ at a given center-of-mass energy is simply the product of the Gaussian center-of-mass energy distribution and the p-wave Breit-Wigner, shown in Figure A1. The resulting distribution is nearly a Gaussian with a width of 6 MeV. Each B meson carries away half of the energy and thus half of the energy spread, resulting in

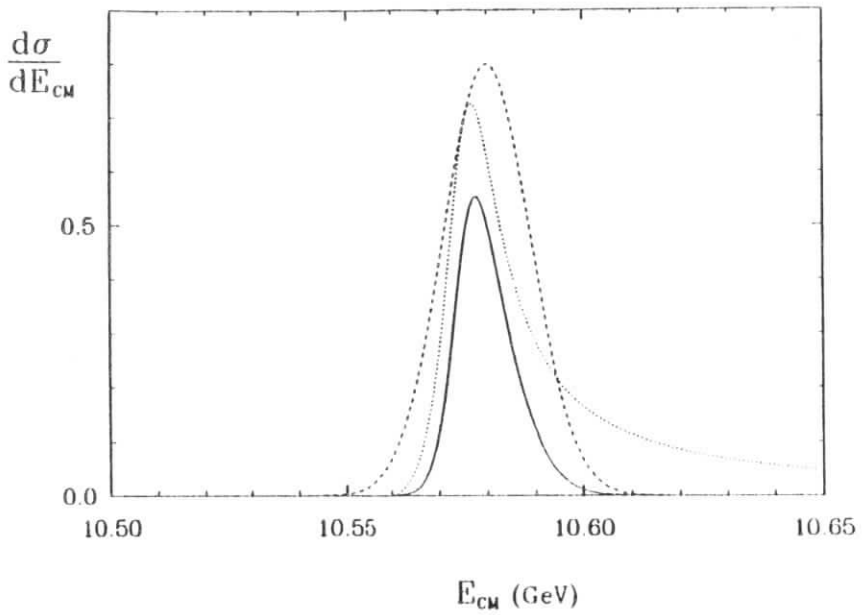

Figure A.1: $\Upsilon(4S)$ production cross section: dashed line = Gaussian for E_{cms} distribution, dotted line = Breit-Wigner of resonance, and solid line = product of both. The scale of $d\sigma/dE_{CM}$ is arbitrary.

an energy resolution of 3 MeV. The spread in the production momentum of the B meson is then $\sigma_P = \sigma_E/\beta \approx 50$ MeV. The total mass resolution is dominated by the spread in the production energy for all decay modes and so the B mass resolution is nearly independent of the decay mode and is

$$\sigma_M = \sqrt{\gamma^2\sigma_E^2 + \gamma^2\beta^2\sigma_P^2} \approx 4MeV.$$

A detailed Monte Carlo yields B mass widths ranging from 3.9 MeV to 4.6 MeV with a statistical error of 0.2 MeV, confirming expectations. Due to uncertainties in the various approximations used all signals are fitted with a fixed width of 4 MeV and assigned a systematic error of 15%.

Appendix B

Reconstruction efficiency correction for $\bar{B} \to D\rho^-$

The procedure for dealing with multiple B candidates in the same event is to choose the candidate with the maximum total probability. This procedure can produce systematic uncertainties in the true number of B mesons. The reconstuction efficiencies can be affected in two ways: 1) loss of genuine B's because an alternate hypothesis, which contributes to the background outside of the B signal, has a higher probability, 2) an artificial increase in the B signal due to the substitution of a spurious low momentum particle for the correct undetected one. The first effect was found to be negligible in Monte Carlo studies for all decay modes investigated. The second effect was found to be problematic for the decays $\bar{B} \to D\pi^-\pi^0$ due to copious production of low momentum photons in B decays, $< n_\gamma >= 5.0 \pm 0.3 \pm 0.3$ [19].

The effect of substituting a spurious low momentum photon for the real one in the reconstruction of π^0's for B reconstruction, can be determined from Monte Carlo studies. Forcing one B meson to decay to $D\rho^-$ and the other to decay freely according to the LUND 6.2 fragmentation scheme [24] approximates the environment of the actual $\Upsilon(4S)$ decays. Applying the reconstruction selection criteria to the data results in a B signal which is 1.30 ± 0.05 times larger than the number obtained by matching the reconstructed decays to the generated

decays. But this enhancement was not trusted due to the large photon yield, $< n_\gamma >= 7.4$, generated by the LUND 6.2 program for B meson decays.

The procedure chosen to obtain a realistic correction was to obtain a clean sample of tagged B meson decays from the data, store the photons observed in the remainder of the event into particle buffers as is done for event mixing, then throw out the photons generated by LUND 6.2 and replace them with the data photons stored in the particle buffers. Since the photons are nearly isotropically distributed in B decays the replacement doesn't require any kinematic rotations or boosts. Then the selection criteria were again applied for the reconstruction of $\bar{B} \to D\rho^-$ and yields the open histogram shown in Figure B1. The shaded histogram represents the correctly identified B mesons. A fit yields an enhance-

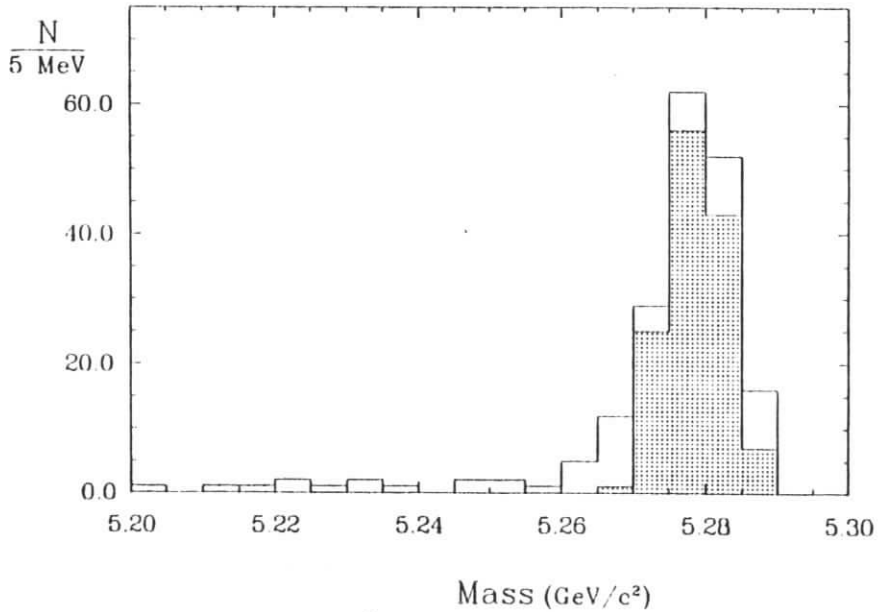

Figure B.1: Enhancement of $\bar{B} \to D\rho^-$ signal. The open histogram represents candidates satisfying the B selection criteria and the shaded histogram represents correctly identified B mesons.

ment of 1.20 ± 0.05, not much different from the value obtained with Monte Carlo data alone. We use an acceptance-correction factor 1.2 ± 0.1 for the B decays to $D\rho^-$ and $D\rho'^-$ reconstructed with two cluster π^0's. No other decays investigated required such a correction.

Appendix C

Helicity angle acceptance-correction

In order to obtain the acceptance-corrected helicity angle distribution of the ρ^- decay coming from $\bar{B} \to D\rho^-$, a reliable and smooth correction function was needed. To obtain this a Monte Carlo was used to generate the decays $\bar{B} \to D\rho^-$ with isotropic ρ^- decays. The method of reconstruction is identical to the selection criteria decribed in chapter 3. The number of ρ^- decays reconstructed with two cluster π^0's per bin of $cos\theta_\pi$ was divided by the number per bin generated to obtain the distribution shown in Figure C1. This was then fitted with a smooth polynomial function to reduce the statistical fluctuations. For the decay $\bar{B} \to D\rho'^-$ the distribution is very similar, although fitted separately for the acceptance determination. No significant correlations of this distribution with the D reconstruction are observed for completely reconstructed B mesons. The fitted curve shown was used to correct the helicity angle distribution to obtain the corrected distribution (Figure 3.4) which shows the characteristic $cos^2\theta_\pi$ behavior expected. To enhance the B signal, a cut $|cos\theta_\pi| > 0.4$ was applied to the two cluster π^0 candidates with the result that 86% of the $D\rho^-$ decays and 88% of the $D\rho'^-$ decays were retained. For single cluster π^0's the cut $cos\theta_\pi > 0.6$ results in the retention of 80% for both the $D\rho^-$ and $D\rho'^-$ decays.

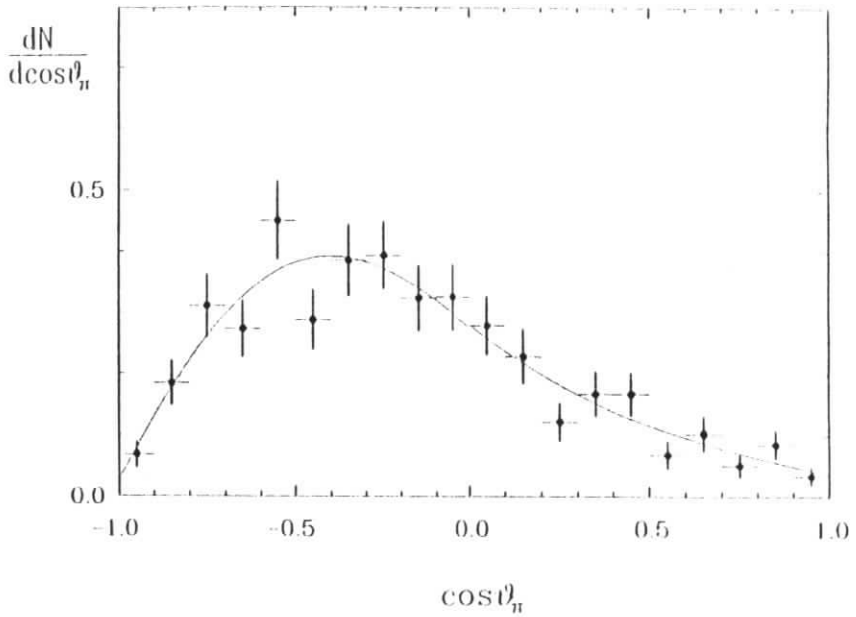

Figure C.1: The ρ^- helicity angle acceptance distribution

Bibliography

[1] S.W. Herb et al., Phys. Rev. Lett. **30** (1977) 252.

[2] C. Berger et al. (PLUTO collaboration), Phys. Lett. **76B** (1978) 243.
C.W. Darden et al. (DASP II collaboration), Phys. Lett. **76B** (1978) 246.
J.K. Bienlein et al. (PLUTO collaboration), Phys. Lett. **78B** (1979) 351.
C.W. Darden et al. (DASP II collaboration), Phys. Lett. **78B** (1979) 364.

[3] D. Andrews et al. (CLEO collaboration), Phys. Rev. Lett. **45** (1980) 219.
G. Finocchiaro et al. (CUSB collaboration), Phys. Rev. Lett. **45** (1980) 222.
K. Berkelman, Phys. Rep. **98** (1983) 145.

[4] G. Zweig, CERN Report 8419/TH.412 unpublished (1964), reprinted in Developments in the Quark Theory of Hadrons, Vol.1: 1964-1978, ed. by D.B. Lichtenberg and S.P. Rosen, Hadronic Press, Nonantum, Massachusetts, (1980) p.22.

[5] Particle Data Group, Phys. Lett. **170B** (1986).

[6] Particle Data Group, Phys. Lett. **204B** (1988).

[7] M. Kobayashi and T. Maskawa, Prog. Theor. Phys. **49** (1973) 653.

[8] H. Albrecht et al. (ARGUS collaboration), Phys. Lett. **192B** (1987) 245.

[9] S.L. Wu, Proc. Int. Symp. on Lepton and Photon Interactions at High Energies (1987) p. 39.

[10] W. Schmidt-Parzefall, Proc. Int. Symp. on Lepton and Photon Interactions at High Energies (1987) p. 257.

[11] M. Fierz, Z. Phys. **88** (1934) 161.

[12] M. Bauer, B. Stech, M. Wirbel, Z. Phys. **C34** (1987) 103.

[13] M. Wirbel, B. Stech, M. Bauer, Z. Phys. **C20** (1985) 637.

[14] F. Hussain and M.D. Scadron, Phys. Rev. **D30** (1984) 1492.

[15] A. Ali, J.G.Körner, G.Kramer, Z. Phys. **C1** (1979) 269.

[16] J.G.Körner, Proc. Int. Symp. on Production and Decay of Heavy Hadrons (1986) p. 279.

[17] J.G.Körner and G.A.Schuler, Z. Phys. **C38** (1988) 511.

[18] M. Shifman, Proc. Int. Symp. on Lepton and Photon Interactions at High Energies (1987) p. 289.

[19] B. Gittelman and S. Stone (CLEO collaboration), Cornell preprint CLNS 87/81 (1987).

[20] R.H. Schindler et al. (MARK II collaboration), Phys. Rev. **D24** (1981) 78.

[21] J. Adler et al. (MARK III collaboration), Phys. Rev. Lett. **60** (1988) 89.

[22] J. Adler et al. (MARK III collaboration), Phys. Lett. **208B** (1988) 152.

[23] H. Albrecht et al. (ARGUS collaboration), Nucl. Inst. and Meth. **A275** (1989) 1.

[24] T. Sjostrand, Phys. Lett. **142B** (1984) 420.
T. Sjostrand, Nucl. Phys. **B248** (1984) 469.

[25] H. Gennow, DESY report F15-85-02 (1985).

[26] J.D. Jackson, Nuovo Cimento **34** (1964) 1644.

[27] H. Albrecht et al. (ARGUS collaboration), Phys. Lett. **185B** (1987) 218.

[28] C. Bebek et al. (CLEO collaboration), Phys. Rev. **D36** (1987) 1289.

[29] H. Albrecht et al. (ARGUS collaboration), Phys. Lett. **197B** (1987) 452.

[30] H. Albrecht et al. (ARGUS collaboration), Phys. Lett. **199B** (1987) 451.

[31] D. Gingrich (ARGUS collaboration), Ph.D. thesis, University of Toronto (1988).

[32] A. Jawahery et al. (CLEO collaboration), submitted to the XXIV Int. Conf. on High Energy Physics, Munich 710,715,716 (1988).

[33] D. Bortoletto et al. (CLEO collaboration) Phys. Rev. **D35** (1987) 19.

[34] G. Harder (ARGUS collaboration), Ph.D. thesis, Hamburg University, unpublished (1989).

[35] H. Albrecht et al. (ARGUS collaboration), Phys. Lett. **219B** (1989) 121.

[36] D.M. Coffman (MARK III collaboration), Proc. AIP Int. Conf. on Hadron Spectroscopy, Maryland (1985) p. 322.

[37] M.S. Witherell (Tagged Photon Spectrometer collaboration) Proc. XXIV Int. Conf. on High Energy Physics, Munich (1988) p. 478.

[38] A. Lindner (ARGUS collaboration), Diploma thesis, Dortmund University, unpublished (1988).